



Interpreting the Spectrotemporal Properties of the Black Hole Candidate Swift J151857.0-572147 during Its First Outburst in 2024

Kaushik Chatterjee^{1,4} , S. Pujitha Suribhatla^{2,3} , Santanu Mondal³ , and Chandra B. Singh¹ ¹ South-Western Institute For Astronomy Research, Yunnan University, University Town, Chenggong, Kunming 650500, People's Republic of China; mails.kc.physics@gmail.com, kaushik@ynu.edu.cn² University of Rome Tor Vergata, Via Cracovia, 90, 00133 Roma RM, Italy³ Indian Institute of Astrophysics, II Block, Koramangala, Bengaluru 560034, Karnataka, India

Received 2024 October 17; revised 2025 April 11; accepted 2025 May 2; published 2025 June 27

Abstract

The transient Galactic black hole candidate Swift J151857.0-572147 went through an outburst in 2024 March for the first time. Using publicly archived Insight-HXMT data, we have analyzed the timing and spectral properties of the source. We have extracted the properties of the quasiperiodic oscillations (QPOs) by fitting the power density spectrum, which inferred that the QPOs are of type C. We have detected QPOs up to ~ 48 keV using an energy dependence study of the QPOs. A high-frequency QPO was not observed during this period. We also conclude that the oscillations of the shock in transonic advective accretion flows may be the possible reason for the origin of the QPOs. In the broad energy band of 2–100 keV, simultaneous data from the three onboard instruments of Insight-HXMT were used to perform spectral analysis. Different combinations of models, including a broken power law, a multicolor disk blackbody, interstellar absorption, nonrelativistic reflection in both neutral and ionized medium, and relativistic reflection, were used to understand the spectral properties during the outburst. We discovered that at the beginning of the analysis period, the source was in an intermediate state and later transitioning toward the soft state based on the spectral parameters. It has a high hydrogen column density, which could be due to some local absorption by the source.

Unified Astronomy Thesaurus concepts: X-ray binary stars (1811); Black holes (162); Stellar accretion disks (1579); Shocks (2086); Compact radiation sources (289); Compact objects (288)

1. Introduction

Black hole (BH) X-ray binaries (BHXRBs) are quite common and important astronomical binary systems. Since accretion serves as the power source in these systems, it is crucial to understand them (J. Frank et al. 2002). In BHXRBs, there is a BH at the center and a companion star orbiting around. They are classified into two main types based on the companion's mass: low-mass BHXRBs (LMBHXRBS) and high-mass BHXRBs (HMBHXRBS; R. A. Remillard & J. E. McClintock 2006). In LMBHXRBS, the compact object is more massive and known as the primary, whereas the companion is the secondary object. Transient and persistent sources are the other categories into which BHXRBs are divided, based on the type of variability in their outbursts. While BH transient sources occasionally exceed detection levels and primarily remain in quiescence, or the dormant state ($L < 10^{32}$ erg s⁻¹; D. C. Hannikainen et al. 2005 and references therein), the flux or count rate of persistent sources remain higher than the detection level most of the time ($L > 10^{36}$ erg s⁻¹; W. Chen et al. 1997 and references therein). Transient sources experience outbursts that can endure for several weeks or even months (B. E. Tetarenko et al. 2016). Though the population of transient HMXBs is increasing, the majority of reported transients are LMXBs (R. A. Remillard & J. E. McClintock 2006; J. E. McClintock et al. 2014 for a review as well). D. Debnath et al. (2010) classified the BH outbursts into

two main categories based on their nature: slow rise, slow decay (SRSD) and fast rise, slow decay (FRSD). G. B. Zhang et al. (2019) divided outbursts into several types, such as glitter, reflare, multipeak, minioutburst, or new outburst, based on their rebrightening characteristics.

The multicolor thermal blackbody and the hard nonthermal power-law components combine to form the spectrum of a BH. The origin of the hard component can be explained by the Comptonizing region, also known as the “Compton cloud,” which is the repository of hot electrons (K. S. Thorne & R. H. Price 1975; R. A. Sunyaev & L. G. Titarchuk 1980, 1985). Over the years, many models have been put forward to explain the composite spectrum of BHXRBs. For example, the standard disk model (N. I. Shakura & R. A. Sunyaev 1973, or SS73), the thick disk model (B. Paczynski & P. Wiita 1980), the advection-dominated accretion flow (ADAF; S. Ichimaru 1977; R. Narayan & I. Yi 1994), and the two-component advective flow (TCAF) model (S. K. Chakrabarti & L. G. Titarchuk 1995) were proposed to explain variabilities in BHXRBs. The soft component is modeled as the radiation coming from the disk, which was explained well by the SS73 disk. However, the model could not describe the harder part of the spectrum. The thick disk model could explain the hard-power-law part of the spectrum. This model is relevant for high-luminosity states, where radiation pressure dominates. However, advection was not taken into consideration in this model. In the ADAF model, the energy generated due to viscous dissipation is advected to the BH and is radiatively inefficient. This model produces a power-law spectrum; however, the direct spectral fitting and explaining the spectral and timing properties are still lacking. Alternatively, the TCAF model solves flow equations and couples them with the radiative transfer processes to

⁴ Corresponding author.



explain both spectral and timing properties simultaneously (S. K. Chakrabarti & L. G. Titarchuk 1995, D. Molteni et al. 1996, S. Mondal & S. K. Chakrabarti 2013, S. K. Chakrabarti et al. 2015).

During the rising phase of an outburst, BH binaries show four distinct BH spectral states starting from hard state (HS) to hard intermediate state (HIMS), soft intermediate state (SIMS), and soft state (SS; see R. A. Remillard & J. E. McClintock 2006 for a review). An opposite sequence follows in the declining phase. Briefly, a BH's spectral state transition forms a hysteresis loop from HS to SS (in the rising phase) and SS to HS (in the declining phase). There is no significant difference in the energy spectrum between HIMS and SIMS. SIMS is classified mostly based on the presence of type-B quasiperiodic oscillations (QPOs). A source that experiences all four of the aforementioned spectral states during an outburst is known to have a complete outburst. If the source does not go to an SS, it is known to have a failed outburst (B. E. Tetarenko et al. 2016).

Understanding temporal aspects is crucial to understanding the dynamics of the accreting flow around the BHs. The light curves exhibit variabilities in short timescales, on the order of milliseconds to seconds, during an outburst, particularly in the high-energy bands. Variabilities like broadband noise and narrow characteristics in the power density spectrum (PDS) can be observed by the Fourier transformation of the light curve (M. van der Klis 1989; T. Belloni et al. 2002). A power-law function is used to describe the broadband noise, which is dispersed over a wide frequency range. The broadband noise can also be fitted with a set of zero-centered Lorentzians (T. Belloni et al. 2002). Lorentzian profiles can be used to describe the QPOs, which show a power peak in the restricted frequency range (D. Psaltis et al. 1999; M.A. Nowak 2000; T. Belloni et al. 2002). Because of their geometrical origin, low-frequency QPOs (LFQPOs) are frequently detected in BHXRBS. Types A, B, and C are the three categories into which LFQPOs are divided, based on some characteristics such as frequency (ν), Q -value ($= \nu/\delta\nu$, where $\delta\nu$ is the FWHM), (%) rms, etc. (P. Casella et al. 2005). High-frequency QPOs (HFQPOs) can also be seen in BHXRBS, although it is quite rare. Several models have been put forward to understand the origin of QPOs, such as the shock oscillation model (D. Molteni et al. 1996; S. K. Chakrabarti et al. 2005, 2008, 2015), magnetoacoustic waves (L. Titarchuk et al. 1998), accretion-ejection instability (M. Tagger & R. Pellat 1999), Lense-Thirring precession (L. Stella et al. 1999; A. Ingram et al. 2009), precessing inner flow model (A. Ingram et al. 2009), corrugation modes (S. Kato & J. Fukue 1980; R.V. Wagoner 1999; S. Kato 2001; D. Tsang & I. Butsky 2013), pressure or accretion rate modes (C. Cabanac et al. 2010), variable Comptonization or vKomph model (K. Karpouzas et al. 2021; C. Bellavita et al. 2022; F. García et al. 2022 and references therein), outflow model (P. Reig et al. 2003; D. Giannios et al. 2004; N. D. Kylafis et al. 2020 and references therein), the jet emitting disk-standard accretion disk model (J. Ferreira 1997; J. Ferreira et al. 2022; P.-O. Petrucci et al. 2008; G. Marcel et al. 2019 and references therein), and retrans model (A. Ingram & S. Motta 2019; G. Mastroserio et al. 2021 and references therein). However, to date, the origin of QPOs is still a topic of debate.

One of the characteristics of the TCAF model (S. K. Chakrabarti & L. G. Titarchuk 1995) is the oscillation

of the shock. According to the TCAF model, matter supplied by the companion star can have a Keplerian and a sub-Keplerian distribution of angular momentum. The Keplerian component creates a geometrically thin and optically thick accretion disk on the equatorial plane and flows in on a viscous timescale because of its high viscosity. As the critical viscosity of this matter increases, the accretion disk moves inward. The sub-Keplerian one falls radially in on a freefall timeline and has a less viscous accretion flow. This matter resides both above and below the Keplerian disk. The optically thin sub-Keplerian component produces a shock front at the location where both the centrifugal and gravitational forces balance each other. The shock front is the boundary layer, also known as the CENTrifugal pressure-supported BOUNDary Layer (CENBOL), which behaves as a so-called Compton cloud. The Keplerian component can explain the soft multicolor blackbody component. The CENBOL region upscatters the soft photons from the disk and makes them as hard power-law photons. The shock forms farther away from the BH at the beginning of the outburst, and the Keplerian disk starts forming; therefore, HS is observed. The blackbody photons start increasing as the Keplerian disk moves inward over time. Thereby, cooling increases as a great number of soft photons intercept the CENBOL. Throughout the process, more photons are released, the flux rises, and the source becomes softer. The CENBOL is completely quenched in a high SS, and the disk approaches the innermost stable orbit. The spectrum becomes soft as a result of only the disk photons now contributing to the radiation. Such profiles of spectral state evolution have been observed in several sources in the TCAF scenario (S. Mondal et al. 2014; D. Debnath et al. 2015; A. Jana et al. 2016; K. Chatterjee et al. 2020, 2021, 2023).

Furthermore, this model explains the QPO properties in addition to the spectral features and their evolutions. When the infall and cooling timescales become comparable, a bigger CENBOL (\sim a few $100 r_S$, where r_S is the Schwarzschild radius) in the HS may result in LFQPOs after satisfying the resonance condition of the oscillation of the shock. The CENBOL slowly shrinks in size as the outburst progresses, and the QPO's frequency increases (D. Molteni et al. 1996; S. Garain et al. 2014; S. K. Chakrabarti et al. 2015). Cooling takes over the heating timescale as the SS is approached, the CENBOL gets smaller and eventually quenches, and there is no oscillation. As a result, there is no QPO in the SS (see S. Mondal et al. 2014; D. Debnath et al. 2015; S. K. Chakrabarti et al. 2015). During the whole evolution path, for different sizes of the CENBOL, different types of QPOs are observed.

While examining the correspondence between the spectral and timing properties solely in terms of the features of the light curve, such as the hardness ratio (HR), and the hardness intensity diagram, a strong association is seen (J. Homan et al. 2001; R. P. Fender et al. 2004; S. Motta et al. 2011). Additionally, accretion rate ratio intensity diagrams can also be used to understand the complete cycle of an outburst from the fundamental accretion flow parameters (S. Mondal et al. 2014; A. Jana et al. 2016; K. Chatterjee et al. 2020). The interlinks between spectral and temporal features from a purely observational ground can also be addressed using the rms-intensity diagram (T. Muñoz-Darias et al. 2011) and the hard-intensity diagram (T. Belloni et al. 2005).

First identified by Swift X-Ray Telescope (XRT) as a gamma-ray burst (GRB; GRB 20240303A, J. A. Kennea et al. 2024), the new Galactic transient Swift J151857.0-572147 was found in

Swift Trigger 1218452 (GCN 35849).⁵ However, thereafter, it was determined to be a Galactic transient due to its constant brightness and location in the Galactic plane. The R.A. and decl. of the source were determined to be R.A. (J2000) = 15^h18^m57^s.00 and decl. (J2000) = −57°21′47.″9 based on the optimal source localization utilizing XRT instantaneous onboard localization (J. A. Kennea et al. 2024). On 2024 March 4, during 15 minutes, from 02:13:13.3 to 02:28:08.9 (MJD 60373.1), follow-up radio observations were conducted using the MeerKAT telescope at 1.28 GHz (L band) with a bandwidth of 856 MHz at a flux density of 10 mJy (F. Carotenuto et al. 2024; F. J. Cowie et al. 2024). The source’s nature was identified as consistent with an X-ray binary in the HS by using the inverted radio spectrum ($f(\nu) \propto \nu^\alpha$, where $\nu \sim +0.5$) in conjunction with the photon index. This suggested that the source might be a BH or a neutron star. On 2024 March 9, from UT 10:35:10 to UT 11:06:20 (MJD 60378.45), the Australia Telescope Compact Array (ATCA) simultaneously recorded radio observations at frequencies of 5.5 and 9 GHz (P. Saikia et al. 2024). Additionally, their investigation confirmed the source to be a Galactic BH. Target of opportunity was carried out on this source with an exposure of 1000 s by Swift/XRT following the ATCA, as reported by M. Del Santo et al. (2024). According to M. Del Santo et al. (2024), it was discovered that the combination of the phenomenological disk blackbody (diskbb) and power-law models describes the spectrum quite well. These discoveries also confirmed that the source is a BH. The source was detected by INTEGRAL serendipitously on March 8, 9, 10, and 11 of 2024 (V. Sguera 2024). The 60 cm Robotic Eye Mount telescope observed the source in both optical and near-infrared wavelengths as part of the monitoring program of GRBs (M. C. Baglio et al. 2024). Optical measurements of the source were also carried out by the Las Cumbres Observatory network (P. Saikia et al. 2024).

From the Swift/XRT spectral modeling, J. A. Kennea et al. (2024) found a column density of $N_{\text{H}} = 5.6 \pm 0.06 \times 10^{22} \text{ cm}^{-2}$. Additionally, they observed a power-law photon index of $\Gamma = 1.78 \pm 0.02$. While B. J. Burridge et al. (2024) reported that the source’s distance was $4.48_{-0.47}^{+0.67}$ kpc, with an HI absorption toward it, the absence of positive velocity absorption lines toward other sources in the field of the HI absorption for this source puts an upper limit on the distance as $15.64_{-0.60}^{+0.77}$ kpc. S. Mondal et al. (2024) reported the mass of the source to be $\sim 9.2 \pm 1.6$ – $10.5 \pm 1.8 M_{\odot}$, estimated using the Jet in TCAF model (S. Mondal & S. K. Chakrabarti 2021), where the mass of the BH is a parameter and the distance to the source is a scale factor taken care of by the model normalization. Authors also estimated the possible disk inclination of $\sim 35^\circ \pm 7^\circ$ – $46^\circ \pm 15^\circ$ with an average spin parameter of 0.65 estimated using the KERRBB model (L.-X. Li et al. 2005) for a given distance of 10 kpc. Since there is no confirmed distance estimation for this source, the authors have adopted an average value from the broad range of proposed distances in the literature. Therefore, the estimation of the spin may vary for different source distance values, requiring further modeling with a confirmed source distance.

Table 1
List of Data Used

Obs. Id. ^[1] (1)	Start UT ^[2] (2)	End UT ^[2] (3)	Exp. (s) ^[3] (4)
P0614374001	2024-03-04 20:08:55	2024-03-06 02:13:33	108,278
P0614374002	2024-03-06 02:13:31	2024-03-08 01:43:18	170,987
P0614374003	2024-03-08 01:43:22	2024-03-10 02:48:37	176,715
P0614374004	2024-03-10 02:48:37	2024-03-12 00:47:47	165,550
P0614374005	2024-03-12 10:14:15	2024-03-12 19:53:12	34,737
P0614374006	2024-03-13 09:59:33	2024-03-15 09:32:39	171,186
P0614374008	2024-03-17 12:09:52	2024-03-17 21:39:51	34,199

Note. Column (1) lists each observation ID. In columns (2) and (3), we give the start and end date and time of each observation ID. Column (4) gives the exposure time of each observation ID.

2. Observation and Data Reduction and Analysis

This source has recently been observed by the Swift satellite and confirmed to be a BH candidate on 2024 March 10 (M. Del Santo et al. 2024). After its discovery and confirmation, it was monitored by various other X-ray satellites, e.g., NICER, NuSTAR, and IXPE. We use X-ray data from China’s first X-ray satellite mission, Insight-HXMT (S.-N. Zhang et al. 2020). After the onset of the outburst, seven observation IDs were available publicly when we started our analysis. We list the data in Table 1 below.

Each of these observation IDs has multiple exposures (up to 14 for some). While listing our analysis results, we will list all those exposure IDs with MJD. Using raw data from all these obs IDs, we first produced science-analyzable, cleaned data, and then performed our analysis. We discuss data reduction and analysis in the following subsections.

2.1. Data Reduction

Following the on-demand retrieval of level-1 data from the repository, we generated cleaned level-2 data for scientific study. The raw data cleaning procedure was carried out as follows. With the HXMTDAS^{6,7} (version 2.05) software, we execute the `hpipeline` command using appropriate input and output directories. For each of the three instruments, this pipeline executes a series of automatic commands. However, there are a few prerequisites that must be met. Specific parameters were established to achieve good time interval, such as elevation angle $>10^\circ$, geomagnetic cutoff rigidity >8 GV, pointing offset angle <0.04 , and distance from the South Atlantic Anomaly >600 s. To facilitate background analyses, each telescope carries large and small field-of-view (FOV) detectors. The small FOV detectors are more suitable for pointing observation as they have a lower probability of source contamination.⁸ Together, these commands extract, clean, and produce science products that are ready for analysis. The HXMT Manual⁹ contains a detailed discussion on this. The spectra for the HE, ME, and LE instruments are generated using the particular commands `hespecgen`, `mespecgen`, and `lespecgen`. On the other hand, the light curve files for the three instruments are created

⁵ <https://gcn.nasa.gov/circulars/35849>

⁶ <http://hxmtcn.ihep.ac.cn/software.jhtml>

⁷ <http://hxmt.org/index.php/usersp/dataan>

⁸ <http://hxmtcn.ihep.ac.cn/AboutHxmt.jhtml>

⁹ <http://hxmtcn.ihep.ac.cn/SoftDoc/501.jhtml>

using the commands `helcgen`, `melcgen`, and `lelcgen`. Appropriate response files are generated by `hercspgen`, `merspgen`, and `lerspgen`. The commands `hebkmap`, `mebkmap`, and `lebkmap` for instruments HE, ME, and LE, respectively, were used to do the background subtraction for both the timing and spectral data. We group the spectrum using the `grppha` task of `FTOOLS` to a minimum of 30 counts per bin for χ^2 fit statistics in `XSPEC`. Additionally, to generate appropriate light curves for PDS generation and QPO search, we adjusted the time bin size to 0.01 s. To search for HFQPOs, we also produced 1 ms time-binned light curves for all the available exposures. The HE light curve covers a broad range of 27–250 keV. To check the energy dependence of QPOs, we produced 0.01 s time-binned HE light curves in seven different energy bands (27–35, 35–48, 48–67, 67–100, 100–150, 150–200, 200–250 keV). Along with this, we also cut light curves in the 48–250 keV energy band for all the HE exposures. The reason for this will be discussed in later sections.

Detailed analysis using these cleaned light curves and spectra files is discussed in the next subsection.

2.2. Data Analysis

We conducted spectral and temporal research on the BH candidate (BHC) Swift J151857.0-572147’s very first outburst in 2024. First, we created 0.01 s time-binned light curves using data from the LE, ME, and HE modules of the HXMT. The fast Fourier transformation in the `powspec` task of the `XRONOS` package in the `HEASoft` software was used to construct the PDS based on those light curves. The data from each observation were split up into many intervals, with 8192 new bins in each interval. To create the final PDS, the PDS for each interval must first be generated and then averaged. The PDS is normalized using the Leahy normalization (D. A. Leahy et al. 1983). A geometrical rebinning of -1.02 is applied. We used these procedures to look for LFQPOs. Initially, the analysis was done without subtracting the white noise. With the concern that it may affect the QPO properties, we have rechecked the analysis by considering the white noise subtraction by running the `powspec` task to produce the PDS using `norm=-1`. In both cases, using the combination of either power-law, constant, and Lorentzian or multiple Lorentzian models, we fit all the features of the full PDS continuum from 0.01 to 50 Hz, including the fundamental QPO and harmonic (if present) features. We also estimated several QPO properties such as frequency (ν_{qpo}), FWHM, and normalization. We found that the normalization of the fundamental QPO barely changes when we use white noise subtraction compared to when we do not consider white noise subtraction. The normalization value stays well within the error range. The effect of white noise is negligible due to the fact that the S/N of the narrow fundamental QPO feature is high enough to make the contribution from the white noise negligible. We report the results in the next section. We found a sharp peak at the position of $2 \times \nu_{\text{qpo}}$ Hz for some observations, which happen to be the harmonic of the fundamental QPO. We used an additional Lorentzian model to fit the harmonic peak. We have extracted their properties from the Lorentzian model fitting. We fitted the PDS of all the exposures for three energy bands: LE (2–10 keV), ME (10–35 keV), and HE (27–250 keV) of the listed seven observations (Table 1). We discuss them later in the Results section.

We also studied the energy dependence of the PDS using only the HE light curves. As mentioned above, we extracted 0.01 s time-binned HE light curves into seven different energy bands (mentioned in the data reduction section) as HE covers a large energy range. We searched for only those exposures in which an LFQPO was present at the full energy band. Using those seven light curves separately, we produced the PDS in the same way as mentioned above. Using the same model approach, we extracted QPO information like ν_{qpo} , FWHM, and normalization. We also did the same for the 48–250 keV HE light curve.

Using these QPO properties (ν_{qpo} , FWHM, norm), we also estimated some properties of the QPOs, like Q -value, rms (%), which help designate their nature. We have also estimated the QPO significance in the result section following H. Sreehari et al. (2019).

We also used all three modules (LE, ME, and HE) for spectral analysis, fitting the broadband data in the 2–100 keV energy range. First, we tried to do the spectral analysis using a combination of simple `diskblackbody` and `power-law` models. However, we did not find an acceptable fit. This is discussed in the Appendix. The combinations of `diskblackbody`, `diskblackbody` broken-power-law models yielded the best fit for the data, according to our search. We have employed the `tbabs` model for interstellar absorption. Since we are simultaneously fitting all three modules, we have included a `constant` to normalize the three resultant fittings. For the LE instrument, we have frozen the constant value to 1 and let the other two constants vary for the ME and HE instruments. These are given in each table of the spectral fitting results in the Appendix, where `constant1` and `constant2` are for the ME and HE instruments, respectively. The following is our best model fit combination: `constant * tbabs * (diskbb + brokenpowerlaw)`. We take this as our Model-1. We also tried to analyze spectral data using the reflection model `pexrav`. For that, our model combination reads as: `constant * tbabs * (diskbb + pexrav)`. We take this as our Model-2. We also tried to use the reflection model `pexriv`, which accounts for ionized medium. Thus, `constant * tbabs * (diskbb + pexriv)` reads as our Model-3. We also performed the spectral fitting using the relativistic `relxill` model (T. Dauser et al. 2016), using the model combination as `constant * tbabs (diskbb + relxill)`. We take this as Model-4. Systematic errors were added to perform spectral analysis, as suggested in the HXMT manual. Not every exposure ID of the specified observation IDs was subjected to spectral analysis. We did not spectrally analyze every exposure, compared to the time analysis. Table 2 indicates the spectrally analyzed exposures with a “*.” This is because, in the case of timing analysis, we observed variations in the timing properties in a single day, but in the case of spectrum analysis, the properties do not significantly change over a short period. We include them in the section on results.

3. Results

We discuss our results from the timing and spectral analysis in the following subsections. However, before going into the analysis results, we discuss the variation in the flux of the source during the outburst first below.

Table 2
Time and Count Rates of All HXMT Exposures

Exposure ID (1)	MJD			Source Count Rate			Background Count Rate		
	Start (2)	Stop (3)	Average (4)	LE (5)	ME (6)	HE (7)	LE (8)	ME (9)	HE (10)
P061437400101-20240304-01-01*	60373.83	60373.96	60373.90	536.58	138.35	570.52	10.86	23.95	404.71
P061437400102-20240304-01-01	60373.96	60374.10	60374.03	580.17	156.85	624.12	10.96	24.83	523.82
P061437400103-20240305-02-01	60374.10	60374.47	60374.29	623.90	159.03	567.25	11.07	23.00	375.57
P061437400104-20240305-02-01	60374.47	60374.60	60374.54	637.14	140.78	522.86	10.54	22.75	357.61
P061437400105-20240305-02-01	60374.60	60374.74	60374.67	662.66	140.50	585.67	10.31	25.13	442.21
P061437400106-20240305-02-01	60374.74	60374.88	60374.81	644.42	132.14	541.91	10.74	21.73	404.61
P061437400107-20240305-02-01*	60374.88	60375.09	60374.98	632.28	130.30	552.83	10.73	24.15	397.43
P061437400201-20240306-01-01	60375.09	60375.46	60375.27	622.66	126.47	523.01	10.95	22.51	380.94
P061437400202-20240306-01-01	60375.46	60375.59	60375.52	595.72	130.94	535.99	10.65	22.87	382.38
P061437400203-20240306-01-01	60375.59	60375.73	60375.66	600.56	139.07	621.86	10.96	25.96	423.93
P061437400204-20240306-01-01	60375.73	60375.87	60375.80	599.74	139.67	575.39	10.65	22.71	397.88
P061437400205-20240306-01-01*	60375.87	60376.01	60375.94	595.50	131.44	555.10	11.40	24.49	403.45
P061437400206-20240307-02-01	60376.01	60376.45	60376.23	608.29	133.40	535.65	11.06	22.87	377.09
P061437400207-20240307-02-01	60376.45	60376.58	60376.51	621.09	129.42	522.51	11.19	22.66	366.92
P061437400208-20240307-02-01	60376.58	60376.72	60376.65	604.54	113.97	550.91	10.61	24.82	436.03
P061437400209-20240307-02-01	60376.72	60376.86	60376.79	638.58	108.06	500.53	10.37	22.94	398.94
P061437400210-20240307-02-01*	60376.86	60377.07	60376.96	666.77	98.46	493.26	11.88	23.53	425.96
P061437400301-20240308-01-01	60377.07	60377.37	60377.22	633.28	103.44	473.36	10.53	21.98	375.15
P061437400302-20240308-01-01	60377.37	60377.50	60377.43	669.41	117.44	481.87	11.93	23.36	374.84
P061437400303-20240308-01-01	60377.50	60377.63	60377.56	625.12	113.95	518.43	11.07	27.79	396.08
P061437400304-20240308-01-01	60377.63	60377.78	60377.70	605.70	106.46	510.03	10.22	22.89	410.33
P061437400305-20240308-01-01	60377.78	60377.91	60377.85	600.03	92.76	473.50	10.47	22.67	391.08
P061437400306-20240308-01-01*	60377.91	60378.05	60377.98	627.36	92.00	472.99	10.61	23.77	419.09
P061437400307-20240309-02-01	60378.05	60378.36	60378.21	651.44	82.46	416.10	10.34	21.32	372.58
P061437400308-20240309-02-01	60378.36	60378.49	60378.42	...	77.33	409.98	...	24.98	355.93
P061437400309-20240309-02-01	60378.49	60378.62	60378.55	598.49	79.97	446.97	11.36	25.21	366.72
P061437400310-20240309-02-01	60378.62	60378.77	60378.69	642.67	87.64	460.32	10.32	23.54	421.21
P061437400311-20240309-02-01*	60378.77	60378.90	60378.83	613.15	98.77	473.44	10.27	23.16	387.30
P061437400312-20240309-02-01	60378.90	60379.11	60379.01	600.63	105.11	489.30	10.49	23.10	402.28
P061437400401-20240310-01-01	60379.11	60379.25	60379.18	602.94	96.22	455.29	10.20	22.20	375.02
P061437400402-20240310-01-01	60379.25	60379.38	60379.31	565.28	93.30	451.50	10.00	22.68	357.27
P061437400403-20240310-01-01	60379.38	60379.51	60379.44	...	108.09	467.63	...	26.14	357.47
P061437400404-20240310-01-01	60379.51	60379.64	60379.58	555.07	115.94	515.31	11.10	27.98	416.68
P061437400405-20240310-01-01	60379.64	60379.77	60379.71	537.59	113.94	521.13	10.30	23.27	415.00
P061437400406-20240310-01-01*	60379.77	60379.90	60379.84	509.38	104.94	503.53	10.25	24.60	378.08
P061437400407-20240310-01-01	60379.90	60380.04	60379.97	517.66	97.23	502.49	10.53	23.50	405.01
P061437400408-20240311-02-01	60380.04	60380.17	60380.10	527.40	90.35	465.21	10.32	21.46	376.86
P061437400409-20240311-02-01	60380.17	60380.30	60380.23	571.07	106.01	462.14	9.93	22.41	360.21
P061437400410-20240311-02-01	60380.30	60380.43	60380.36	548.30	115.14	474.22	10.07	22.07	373.48
P061437400411-20240311-02-01	60380.43	60380.56	60380.50	580.27	134.88	525.68	11.17	29.07	386.17
P061437400412-20240311-02-01	60380.56	60380.69	60380.63	462.08	106.48	537.55	9.94	25.56	420.90
P061437400413-20240311-02-01	60380.69	60380.82	60380.76	477.94	97.35	493.75	10.20	22.13	396.88
P061437400414-20240311-02-01*	60380.82	60381.03	60380.93	474.07	96.15	498.83	10.35	23.93	404.79
P061437400501-20240312-01-01	60381.42	60381.55	60381.49	483.34	68.63	433.63	10.76	26.38	405.46
P061437400502-20240312-01-01	60381.55	60381.68	60381.61	482.73	64.80	445.23	10.16	24.11	424.39
P061437400503-20240312-01-01*	60381.68	60381.82	60381.75	537.66	80.44	417.55	10.13	21.57	402.64
P061437400601-20240313-01-01	60382.41	60382.58	60382.49	510.02	79.82	443.41	10.98	26.42	397.53
P061437400602-20240313-01-01	60382.58	60382.72	60382.65	516.28	82.24	437.49	9.78	23.70	412.44
P061437400603-20240313-01-01	60382.72	60382.86	60382.79	506.55	88.41	435.97	9.95	23.59	391.56
P061437400604-20240313-01-01*	60382.86	60383.00	60382.93	501.54	92.93	460.78	10.00	24.10	401.87
P061437400605-20240314-02-01	60383.00	60383.13	60383.06	446.42	67.57	428.66	10.19	21.78	380.04
P061437400606-20240314-02-01	60383.13	60383.26	60383.19	441.60	69.75	419.85	9.98	21.97	368.76
P061437400607-20240314-02-01	60383.26	60383.39	60383.33	430.38	75.95	434.04	9.76	23.01	355.99
P061437400608-20240314-02-01	60383.39	60383.52	60383.46	494.91	100.00	482.17	11.36	28.54	445.78
P061437400609-20240314-02-01	60383.52	60383.66	60383.59	473.40	97.84	479.17	9.87	24.27	428.51
P061437400610-20240314-02-01	60383.66	60383.79	60383.72	470.76	107.58	473.73	9.83	22.89	400.49
P061437400611-20240314-02-01*	60383.79	60383.92	60383.85	442.65	94.15	520.03	10.68	24.74	411.57
P061437400612-20240314-02-01*	60383.92	60384.05	60383.98	405.67	84.88	471.21	10.46	22.74	395.89
P061437400613-20240315-03-01*	60384.05	60384.18	60384.12	385.96	84.14	459.38	10.01	22.73	376.74
P061437400614-20240315-03-01	60384.18	60384.39	60384.29	408.51	80.65	438.74	9.89	22.18	366.30
P061437400801-20240317-01-01*	60386.50	60386.67	60386.59	265.65	36.99	421.11	9.68	22.76	404.34
P061437400802-20240317-01-01	60386.67	60386.91	60386.79	256.75	43.10	440.27	9.88	24.65	422.77

Notes. Column (1) represents the Exposure IDs, taken for this complete analysis. Columns (2) and (3) represent the start and end MJDs of those exposures, respectively. Column (4) represents the average MJD for those exposure IDs. Columns (5), (6), and (7) represent source count rate in LE, ME, and HE bands. Columns (8), (9), and (10) represent background count rate in LE, ME, and HE bands in “counts s⁻¹” unit.

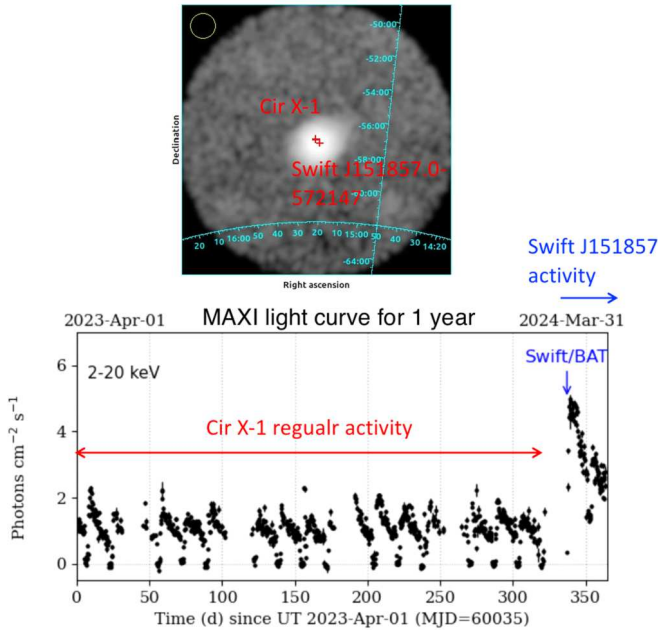


Figure 1. MAXI/GSC FOV and source activity for the sources Cir X-1 and Swift J151857.0-572147 (Credits: MAXI Team).

3.1. Timing Properties

First, we will discuss the outburst evolution from the light curve profiles and HR, and then we will discuss our analysis of QPOs.

3.1.1. Outburst Profile and Hardness Ratio

Although the BHC Swift J151857.0-572147 was observed by the MAXI Gas Slit Camera (GSC) instrument, it was not recognized as a new source by them. The source is located at $\sim 0.2^\circ$ from the source Cir X-1. Although the facility could identify the brightening of the source, the two sources could not be resolved separately. In Figure 1, we show the location of the two sources in the upper panel. It can be noticed that the two sources are located very close to each other. The lower panel of the figure shows increased activity due to the outburst of Swift J151857.0-572147. According to J.-Q. Peng et al. (2024), Cir X-1 was active in the SS during this time. Thus, the contribution from Cir X-1 could have contributed to the low-energy part (i.e., LE) of the light curve.

In Figure 2, we show the variation in the count rates for around 15 days. The count rates are extracted using the LE, ME, and HE light curves of HXMT in the 2–10, 10–35, and 27–250 keV energy bands. In panel (a), we show the variation in those source and background count rates for the three bands (in respective colors). Red is for LE, while green and blue colors are used to represent ME and HE bands. The filled circle (of each color) lines represent the source counts, whereas the triangle-shaped lines represent the background count rates. As can be noticed, the HE background count rate was quite high and was almost comparable to the source count rate. This could be due to the combination of two reasons, e.g., the large effective area of HE and the close proximity of the source to Cir X-1. However, as mentioned earlier, the contribution from Cir X-1 could be in low energy as it was in the SS. Thus, it is hard to comprehend the actual reason behind it. The other two bands showed a significant difference in count levels between

source and background. In Table 2, we list the start, end, and average MJDs of all our analyzed exposures. We also list the source and background count rates for LE, ME, and HE in Table 2. In panel (b) of Figure 2, we show the count rates in 2–4, 4–10 keV energy bands, which are extracted using LE light curves. In panel (c), the HR is plotted using the ratio of the LE count rates of 4–10 to 2–4 keV.

From the light curves, we see that the source has high count rates in all three bands. For Insight-HXMT, a count rate of 800, 500, and 800 counts s^{-1} from LE, ME, and HE corresponds to the flux equivalent to 1Crab. These flux values give an idea of the brightness of the source. From the variation, HR gives a rough idea that the source had already moved past its HS as Insight-HXMT started monitoring the source. As time progressed, the spectral nature progressed from intermediate to softer states. However, we need timing and spectral analysis results to designate this firmly. We discuss them in the next two subsections.

3.1.2. Low-frequency Quasiperiodic Oscillations

We have created the PDS to analyze QPOs using the 0.01 s time-binned light curves from all three bands (LE, ME, and HE), as stated in Section 2. In Figure 3, we show the best model-fitted PDS continuum for the LE band, for both fittings in (a) `powspec`, and (b) `xspec` for the observation ID P0614374001 (exposure ID: P061437400101-20240304-01-01). First, we used the combination of power-law, constant, and Lorentzian models in `powspec`. After the best model fitting, the same is followed in `xspec`. From the `xspec` fitting panel, one can also observe the goodness of fitting, as well as the contributions from various features of the PDS, including the fundamental QPO and harmonic. While both the QPO and harmonic were present in the LE band, the harmonic nature was absent in ME and was not very prominent in HE, as observed from the fittings in all the bands. The QPO and harmonic have a 1:2 ratio in frequency, with the $\nu_{\text{qpo}} \sim 3.19 \pm 0.02$ and $\nu_{\text{harmonic}} \sim 6.43 \pm 0.04$ Hz, respectively. The fundamental and harmonic QPO in this exposure has an FWHM of 0.35 ± 0.05 , 0.39 ± 0.13 , and normalization of 1.84 ± 0.23 , 0.57 ± 0.14 , respectively. We noticed the presence of fundamental QPOs in the PDS of each of the three energy bands. We first checked all the exposures for the observation ID P0614374001. From our fitting, we first extracted the basic QPO information, which is QPO frequency (ν_{qpo}), FWHM, and QPO normalization.

We found that QPO was present in most of the exposures of this observation ID. It was present for all exposures in the ME band and was absent in the last LE band and the second and fifth HE bands. Also, the QPO frequency evolved within a short period of ~ 1.5 days of the duration of this observation ID P0614374001. Thus, we checked for QPOs for all the exposures. At the start of our analysis period, fundamental QPO was present in almost all of the exposures. The ν_{qpo} was ~ 3.2 for all three bands on MJD 60373.9, and it increased as the outburst progressed. Then, after some days, it decreased, and then again showed an increasing trend. Then, it again decreased and increased and decreased and continued this way. The highest frequency in the LE band was 8.1 Hz on MJD 60376.9, on which both the light curves in the ME and HE bands were not created by the `hpipeline` command. The highest frequency in the ME band was 8.97 Hz on MJD 60377.9, on which the LE and ME light curves were not produced. In the HE band, ν_{qpo} was the highest on MJD

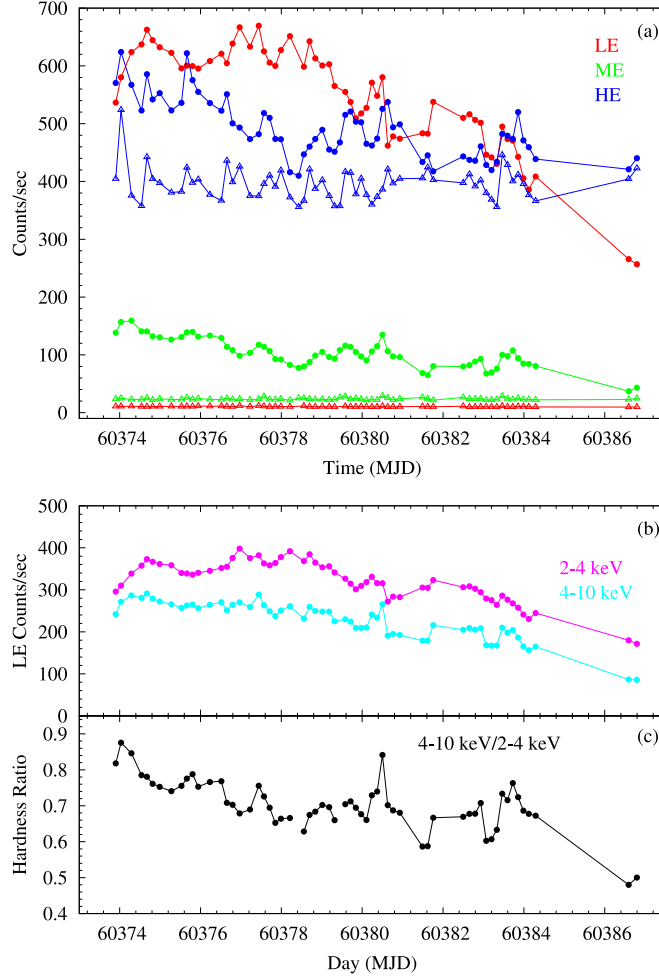


Figure 2. Variation in the Insight-HXMT (a) source and background count rates in LE, ME, and HE bands, (b) 2–4 keV and 4–10 keV LE count rates, (c) HR (4–10 keV/2–4 keV) with time.

60379.3 with a value of 6.82 Hz. We show the variations in the QPO frequency during our full analysis period in Figures 4(a)–(c) for (a) LE, (b) ME, and (c) HE. In Table 3, we listed the values of ν_{qpo} in columns (2), (3), and (4) for LE, ME, and HE. Although for the exposure P061437400103-20240305-02-01, there was a presence of a harmonic nature in the HE band, we did not fit it as the noise was high and the harmonic was like a broad Lorentzian feature. We did not find a harmonic for any other exposures of any other observation ID in any of the three bands.

We were able to extract certain information about QPOs, such as FWHM and normalization, by the use of PDS fitting. For the exposures, we additionally retrieved the source and background count rates. Using the formula from Q.-C. Bu et al. (2015), we estimated the fractional rms as $\text{rms} = \sqrt{\frac{P}{S+B} \frac{S+B}{S}}$, which denotes the fractional variability in the PDS. Here, S and B represent the count rates of the source and the background, respectively. P is the Leahy normalized power. We also estimated the Q -factor ($\nu/\delta\nu$), which measures the sharpness of the QPO. Table 3 lists these values for LE, ME, and HE in columns (5)–(7) (Q -value) and (8)–(10) (rms), respectively. This is shown in Figure 5. The variations in the Q -factor were consistent in the three different bands. To check if there is any correlation between the QPO rms and QPO frequency, we plotted those two properties

against each other in Figure 6. We have not found any correlation between them for this source in all three energy bands.

As explained before, we also checked the energy dependence of QPOs using the HE light curve in seven different energy bands. These energy ranges were chosen to maintain similarity with X. Ma et al. (2023). The PDS continuums for the observation ID P0614374001 (exposure ID: P061437400101-20240304-01-01) are given in Figures 7(a)–(g) for respective energy bands. For this exposure, we find that the fundamental QPO was prominently present at 3.274 Hz in the 27–35 keV energy band, while it is also present in the 35–48 keV with a little change in frequency of 3.222 Hz. However, the nature of QPO was not as strong as in the 27–35 keV. Above 48 keV, we did not find any nature of fundamental QPO. We notice a sharp fall in QPO strength above 48 keV. K. Chatterjee et al. (2021) studied QPO energy dependence for the BHC GRS 1716-249 using AstroSat data. Although the fundamental QPO nature got weaker in high energies in that report, it did not show this type of sharp fall of QPO nature after some energy band. A possible weak harmonic nature was noticed in the 35–48 keV band, which was not present in the 27–35 keV band. However, it looks very weak, and we did not model it. Harmonic nature was also not observed above 48 keV. We checked this for all 31 exposures for which fundamental LFQPO was present in the HE

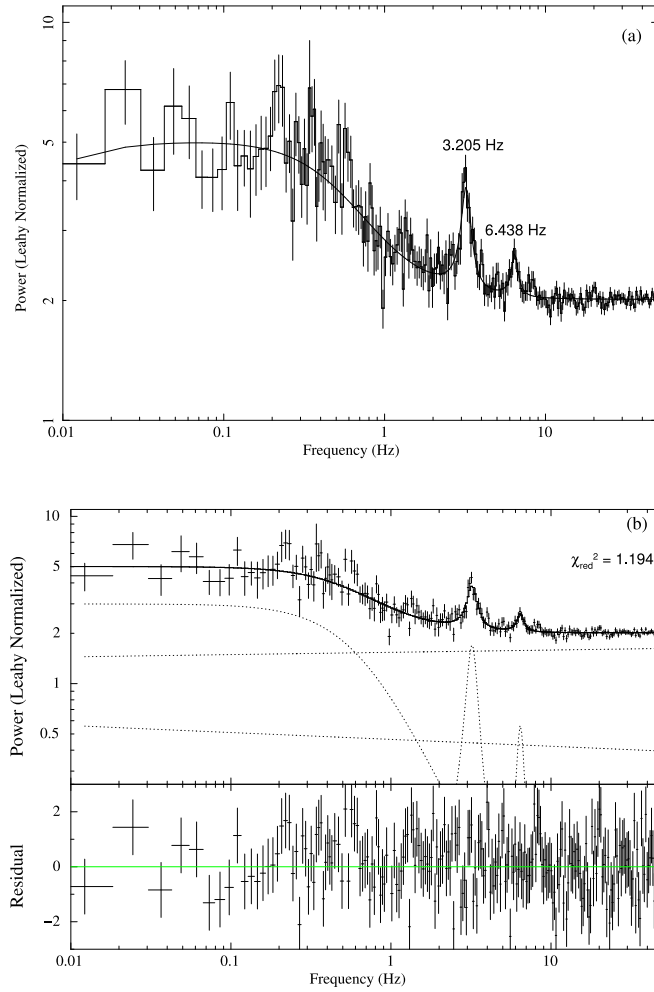


Figure 3. Model-fitted PDS continuum in 0.01–50 Hz for the LE band for fitting in (a) `powspec` and (b) `xspec`. The best fit is achieved using a combination of a set of models: power law, constant, and Lorentzian.

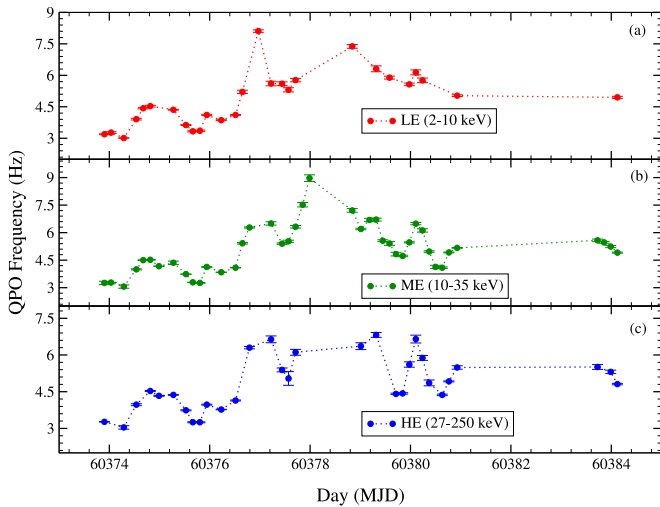


Figure 4. Evolution of QPO frequency with time during the whole period of analysis for (a) LE, (b) ME, and (c) HE.

light curve. We find that for all of these exposures, QPO was absent above 48 keV. For some exposures, we found that LFQPO was absent in the 35–48 keV band, although it was present in the 27–35 keV band.

Using the formulas, as mentioned above, we estimated Q -values and rms (%) for all these exposures in both bands. In Figure 8, we show the variation in the QPO frequency, Q -value, and rms (%) for all these exposures with time. We notice that the ν_{qpo} varied in a very narrow range between these two energy bands, which is within the error range. The Q -value shows a random variation for both the bands, where it was sometimes higher for the 27–35 keV band and sometimes for the 35–48 keV band. The overall variation in the rms (%) was higher in the case of the 27–35 keV band, compared to the higher band. The values of the variation in the QPO properties in the case of energy dependence are given in Table 4.

We also show the variation in the QPO rms with energy in Figure 9. We noticed that the QPO rms was the lowest in the LE band. It was the highest in the ME band. Then it started to decrease. Above 48 keV, we did not find the presence of any QPO.

Apart from this, we also searched for QPOs in the 48–250 keV energy band light curve. As we move to the higher energies, the detector’s effective area decreases. Thus, the number of photons also reduces. However, in high energies (e.g., ~ 50 keV), if the energy range is large, the PDS of the light curve may show the presence of QPOs. This is what we wanted to check. Since above 48 keV, no QPO was found in the PDS, we wanted to make a further consistency check in a

Table 3
Results from Timing Analysis of LE, ME, and HE Light Curves

Time (MJD) (1)	QPO Frequency (Hz)			Q-Value			rms (%)			Significance			Shock Location (X_s)		
	LE (2)	ME (3)	HE (4)	LE (5)	ME (6)	HE (7)	LE (8)	ME (9)	HE (10)	LE (11)	ME (12)	HE (13)	LE (14)	ME (15)	HE (16)
3.90	3.19 ± 0.02	3.25 ± 0.08	3.26 ± 0.01	9.1 ± 1.3	9.0 ± 0.5	9.0 ± 0.7	4.3 ± 0.4	10.8 ± 0.4	5.8 ± 0.3	8.0	17.4	15.4	95.6 ± 9.9	94.2 ± 9.7	94.0 ± 9.7
4.03	3.26 ± 0.04	3.27 ± 0.02	...	7.1 ± 1.5	7.1 ± 0.6	...	4.1 ± 0.5	9.7 ± 0.5	...	6.1	12.6	...	94.0 ± 9.7	93.9 ± 9.7	...
4.28	3.00 ± 0.01	3.05 ± 0.09	3.03 ± 0.07	8.1 ± 0.9	6.5 ± 0.3	7.0 ± 0.3	3.4 ± 0.2	9.6 ± 0.2	6.5 ± 0.1	10.6	25.0	27.1	99.4 ± 9.3	98.3 ± 9.4	98.7 ± 9.5
4.53	3.91 ± 0.04	4.00 ± 0.03	3.97 ± 0.04	6.5 ± 1.4	4.6 ± 0.5	4.1 ± 0.4	3.5 ± 0.4	11.2 ± 0.7	7.3 ± 0.5	6.9	12.6	12.3	83.5 ± 8.6	82.2 ± 8.5	82.6 ± 8.5
4.67	4.42 ± 0.03	4.50 ± 0.02	...	8.5 ± 1.3	6.1 ± 0.5	...	3.6 ± 0.3	11.5 ± 0.6	...	8.3	15.4	...	76.8 ± 7.9	76.0 ± 7.8	...
4.81	4.53 ± 0.04	4.51 ± 0.02	4.53 ± 0.02	7.9 ± 1.7	5.7 ± 0.3	6.6 ± 0.4	3.7 ± 0.4	12.4 ± 0.5	6.5 ± 0.3	6.4	17.8	17.5	75.7 ± 7.8	75.8 ± 7.8	75.7 ± 7.8
4.98	...	4.17 ± 0.02	4.32 ± 0.02	...	6.2 ± 0.3	8.8 ± 1.0	...	12.6 ± 0.4	6.1 ± 0.4	...	21.0	9.7	...	80.0 ± 8.3	78.0 ± 8.0
5.27	4.36 ± 0.02	4.36 ± 0.08	4.36 ± 0.09	9.4 ± 1.2	7.6 ± 0.3	7.6 ± 0.4	3.6 ± 0.2	12.0 ± 0.2	6.3 ± 0.2	10.0	29.0	22.8	77.6 ± 8.0	77.6 ± 8.0	77.5 ± 8.0
5.52	3.63 ± 0.02	3.74 ± 0.02	3.74 ± 0.02	10.6 ± 1.9	8.6 ± 0.8	7.4 ± 0.7	4.0 ± 0.4	11.7 ± 0.7	7.0 ± 0.4	7.6	10.4	10.4	87.7 ± 9.1	86.0 ± 8.9	86.0 ± 8.9
5.66	3.32 ± 0.03	3.28 ± 0.02	3.25 ± 0.02	6.6 ± 1.3	7.4 ± 0.6	12. ± 2.8	3.9 ± 0.4	10.9 ± 0.6	5.3 ± 0.8	6.8	13.5	4.3	92.9 ± 9.6	93.7 ± 9.7	94.4 ± 9.8
5.80	3.35 ± 0.03	3.25 ± 0.02	3.25 ± 0.02	7.0 ± 1.4	4.4 ± 0.2	4.6 ± 0.3	3.6 ± 0.4	11.8 ± 0.5	6.4 ± 0.3	6.5	18.0	16.0	92.4 ± 9.5	94.2 ± 9.7	94.4 ± 9.8
5.94	4.11 ± 0.03	4.13 ± 0.02	3.97 ± 0.02	8.9 ± 2.3	7.0 ± 0.2	11.3 ± 1.6	3.9 ± 0.6	11.5 ± 0.4	5.7 ± 0.5	4.7	13.3	7.6	80.7 ± 8.3	80.5 ± 8.3	82.6 ± 8.5
6.23	3.85 ± 0.02	3.83 ± 0.02	3.76 ± 0.02	6.7 ± 0.9	6.0 ± 0.2	5.6 ± 0.2	3.8 ± 0.3	11.6 ± 0.3	6.7 ± 0.1	10.7	25.5	27.0	84.2 ± 8.7	84.5 ± 8.7	85.5 ± 8.8
6.51	4.11 ± 0.02	4.09 ± 0.02	4.13 ± 0.02	16.4 ± 3.9	12.7 ± 1.5	9.0 ± 1.3	3.3 ± 0.5	11.1 ± 0.9	6.1 ± 0.6	4.3	8.7	7.7	80.7 ± 8.3	81.0 ± 8.4	80.4 ± 8.3
6.65	5.21 ± 0.08	5.42 ± 0.03	...	5.0 ± 1.3	4.2 ± 0.4	...	3.9 ± 0.5	13.6 ± 0.9	...	6.2	12.5	...	68.9 ± 7.1	67.1 ± 6.9	...
6.79	...	6.28 ± 0.02	6.30 ± 0.05	...	7.5 ± 0.8	6.2 ± 1.0	...	11.0 ± 0.7	5.2 ± 0.5	...	12.0	9.6	...	60.9 ± 6.3	60.7 ± 6.3
6.96	8.10 ± 0.06	5.9 ± 0.9	3.8 ± 0.3	11.5	51.3 ± 5.3
7.22	5.61 ± 0.15	6.50 ± 0.09	6.63 ± 0.15	4.6 ± 1.5	2.3 ± 0.2	1.9 ± 0.3	2.7 ± 0.5	13.9 ± 0.8	6.7 ± 0.6	5.0	19.0	11.5	65.6 ± 6.8	59.5 ± 6.1	58.6 ± 6.0
7.44	5.59 ± 0.09	5.40 ± 0.03	5.38 ± 0.08	6.5 ± 2.5	9.3 ± 1.7	4.8 ± 1.0	3.8 ± 0.8	10.6 ± 1.3	7.1 ± 0.9	3.6	5.7	6.6	65.7 ± 6.8	67.3 ± 6.9	67.4 ± 6.9
7.57	5.30 ± 0.09	5.53 ± 0.06	5.03 ± 0.21	17.6 ± 1.7	4.4 ± 0.7	1.4 ± 0.5	2.2 ± 1.1	13.5 ± 1.3	10.0 ± 2.0	3.4	8.6	5.5	68.1 ± 7.0	66.2 ± 6.8	70.5 ± 7.3
7.71	5.76 ± 0.08	6.32 ± 0.06	6.11 ± 0.14	6.1 ± 1.6	3.6 ± 0.5	3.1 ± 0.6	3.4 ± 0.5	12.7 ± 1.0	6.0 ± 0.7	6.0	13.0	8.5	64.4 ± 6.6	60.6 ± 6.2	62.0 ± 6.4
7.85	...	7.51 ± 0.16	3.3 ± 0.5	12.9 ± 1.3	8.7	54.0 ± 5.6	...
7.98	...	8.97 ± 0.18	3.6 ± 0.9	11.6 ± 1.7	6.5	48.0 ± 4.9	...
8.21
8.42
8.55
8.69
8.83	7.38 ± 0.09	7.21 ± 0.09	...	13.6 ± 6.8	4.0 ± 0.7	...	2.1 ± 0.6	11.2 ± 1.2	...	3.2	9.0	...	54.6 ± 5.6	55.5 ± 5.7	...
9.01	...	6.19 ± 0.03	6.36 ± 0.15	...	7.7 ± 1.2	3.8 ± 1.0	...	9.5 ± 0.9	5.7 ± 0.9	...	8.85	5.6	...	61.4 ± 6.3	60.3 ± 6.2
9.18	...	6.69 ± 0.09	5.0 ± 1.1	9.7 ± 1.3	7.2	58.3 ± 6.0	...
9.31	6.30 ± 0.13	6.71 ± 0.07	6.82 ± 0.13	5.6 ± 2.3	5.9 ± 1.3	4.5 ± 0.9	3.1 ± 0.7	10.4 ± 1.4	6.1 ± 0.7	3.8	6.7	8.2	60.7 ± 6.2	58.2 ± 6.0	57.6 ± 5.9
9.44	...	5.55 ± 0.04	11.5 ± 3.3	9.8 ± 1.8	4.3	66.0 ± 6.8	...
9.58	5.88 ± 0.07	5.40 ± 0.13	...	13.4 ± 6.9	4.5 ± 1.2	...	3.0 ± 0.9	10.5 ± 1.6	...	2.8	6.2	...	63.5 ± 6.5	67.2 ± 6.9	...
9.71	...	4.82 ± 0.09	4.40 ± 0.03	...	2.9 ± 0.5	7.7 ± 1.2	...	10.7 ± 1.1	4.9 ± 0.4	...	10.5	9.0	...	72.5 ± 7.5	77.0 ± 7.9
9.84	...	4.73 ± 0.03	4.42 ± 0.03	...	5.2 ± 0.6	7.6 ± 1.3	...	12.0 ± 0.8	5.7 ± 0.6	...	12.4	7.3	...	73.5 ± 7.6	76.8 ± 7.9
9.97	5.57 ± 0.06	5.46 ± 0.02	5.61 ± 0.15	8.0 ± 2.1	7.9 ± 1.0	4.7 ± 1.3	3.8 ± 0.6	11.4 ± 0.9	5.4 ± 0.9	5.3	10.4	5.0	65.9 ± 6.8	66.7 ± 6.9	65.6 ± 6.8
10.10	6.13 ± 0.12	6.48 ± 0.06	6.65 ± 0.16	7.3 ± 3.3	5.8 ± 1.0	3.4 ± 0.9	2.9 ± 0.8	10.9 ± 1.1	5.4 ± 0.8	3.1	8.5	6.2	61.8 ± 6.4	59.5 ± 6.1	58.6 ± 6.0
10.23	5.76 ± 0.10	6.11 ± 0.08	5.88 ± 0.09	5.1 ± 1.6	4.3 ± 0.8	3.7 ± 0.8	3.4 ± 0.6	10.5 ± 1.2	5.8 ± 0.7	5.4	8.8	7.2	64.5 ± 6.6	61.9 ± 6.4	63.6 ± 6.6
10.36	...	4.96 ± 0.04	4.86 ± 0.14	...	8.2 ± 1.7	4.1 ± 1.3	...	9.6 ± 1.3	5.6 ± 1.0	...	6.0	5.1	...	71.1 ± 7.3	72.2 ± 7.4
10.50	...	4.13 ± 0.08	3.8 ± 1.0	11.1 ± 1.8	5.4	80.5 ± 8.3	...
10.63	...	4.09 ± 0.03	4.36 ± 0.03	...	4.4 ± 0.6	9.2 ± 1.7	...	11.7 ± 1.0	5.3 ± 0.6	...	10.3	6.1	...	81.0 ± 8.4	77.5 ± 8.0
10.76	...	4.92 ± 0.02	4.92 ± 0.02	...	8.9 ± 1.1	10.2 ± 1.4	...	10.9 ± 0.8	4.9 ± 0.4	...	11.1	9.0	...	71.6 ± 7.4	71.6 ± 7.4
10.92	5.03 ± 0.04	5.17 ± 0.02	5.48 ± 0.07	7.9 ± 1.5	8.9 ± 1.0	8.3 ± 2.5	3.8 ± 0.4	10.9 ± 0.8	4.2 ± 0.8	6.9	11.3	4.4	70.6 ± 7.3	69.3 ± 7.1	66.6 ± 6.9
11.49
11.61
11.75

Table 3
(Continued)

Time (MJD) (1)	QPO Frequency (Hz)			Q-Value			rms (%)			Significance			Shock Location (X_s)		
	LE (2)	ME (3)	HE (4)	LE (5)	ME (6)	HE (7)	LE (8)	ME (9)	HE (10)	LE (11)	ME (12)	HE (13)	LE (14)	ME (15)	HE (16)
12.49
12.65
12.79
12.93
13.06
13.19
13.33
13.46
13.59
13.72	...	5.57 ± 0.06	5.51 ± 0.13	...	4.9 ± 0.9	3.8 ± 0.8	...	9.4 ± 1.1	5.3 ± 0.7	...	7.5	6.6	...	65.8 ± 6.8	66.4 ± 6.8
13.85	...	5.46 ± 0.04	7.1 ± 1.6	9.4 ± 1.3	6.1	66.7 ± 6.9	...
13.98	...	5.23 ± 0.06	5.30 ± 0.07	...	6.3 ± 1.3	6.6 ± 1.9	...	10.3 ± 1.3	4.5 ± 0.7	...	6.8	5.2	...	68.7 ± 7.1	68.1 ± 7.0
14.12	4.94 ± 0.05	4.90 ± 0.02	4.80 ± 0.03	8.3 ± 2.4	8.4 ± 1.6	8.4 ± 1.6	3.6 ± 0.6	10.4 ± 1.1	4.9 ± 0.5	5.0	8.7	7.7	71.3 ± 7.4	71.7 ± 7.4	72.7 ± 7.5
14.29
16.59
16.79

Note. In column (1), we have listed the MJD-60370 (to save space) of the exposure IDs we used. Columns (2), (3), and (4) represent the QPO frequency (in Hz unit) in LE, ME, and HE energy bands, respectively. Columns (5), (6), and (7) represent the Q -values of QPOs in LE, ME, and HE energy bands, respectively. Columns (8), (9), and (10) represent the QPO rms (%) in LE, ME, and HE energy bands, respectively. Columns (11), (12), and (13) represent the significance of QPO in LE, ME, and HE energy bands, respectively. Columns (14), (15), and (16) represent the shock location in LE, ME, and HE energy bands, respectively. X is in units of Schwarzschild radius ($r = 2GM_{\text{BH}}/c^2$).

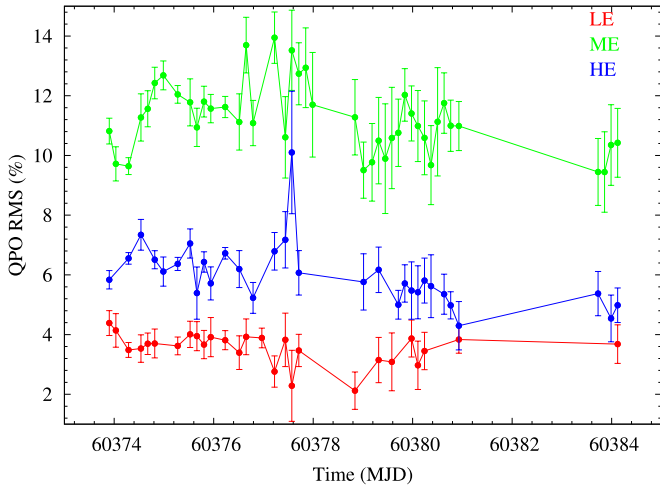


Figure 5. Variation in QPO rms with time for the LE (red), ME (green), and HE (blue) bands, respectively.

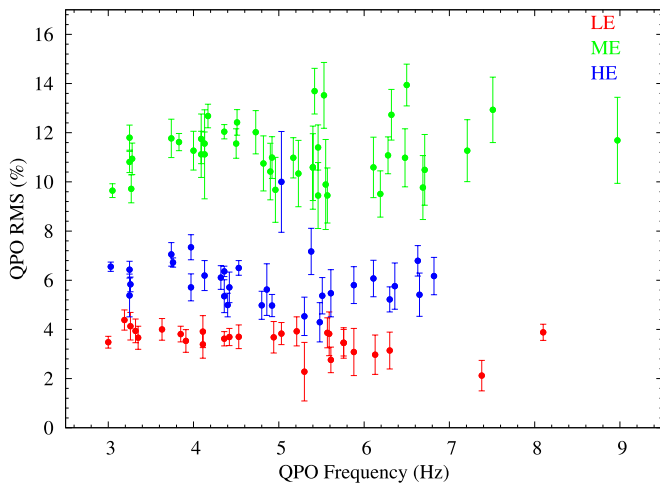


Figure 6. Variation in QPO rms with QPO frequency for the LE (red), ME (green), and HE (blue) bands, respectively.

broader energy band, to see if it shows any QPOs or not. We could not find the presence of QPO in the higher energy bands in any of the exposures, except for the observation ID. P0614374001 with exposure ID. P061437400103-20240305-02-01. We found that a fundamental QPO was present in this exposure at 3.06 ± 0.05 Hz. This is shown in Figure 10. For all the detected QPOs, we have estimated the significance (σ) using the relations given in H. Sreehari et al. (2019). The values of the significance are given in each table where QPO information is listed.

3.1.3. High-frequency QPOs

Apart from looking for LFQPOs, we also searched for HFQPOs in all the light curves for all three bands in all 62 exposures. In Figures 11(a)–(c), we show the PDS continuum for a 0.001 s time-binned (Nyquist frequency = 500 Hz) curve for (a) LE, (b) ME, and (c) HE. However, we did not find any signature of HFQPOs in any of our light curves. The frequency in the PDS in LE, ME, and HE in Figure 11 is similar to that in Figure 3. Those are the LFQPOs present in those light curves during that exposure.

3.2. Spectral Properties

Studying the spectral features sheds additional light on the nature of the outburst in addition to the temporal properties. We examined the source using the Insight-HXMT data that were available for 14 exposures in total. The exposure IDs in Table 2’s first column have a “*” symbol next to them. We perform a thorough spectral study using HXMT data on this source for every consecutive day for the available data. Our spectrum investigation was initiated with MJD 60373.9. For spectral fitting, we have simultaneously analyzed LE+ME+HE in the 2–100 keV energy band (LE in 2–10, ME in 10–35, and HE in 27–100 keV) for all of the chosen exposure IDs.

First, we tried to model the spectrum with simple additive models `diskbb`¹⁰ and `power law`.¹¹ We also used the multiplicative `tbabs`¹² (with Wilm abundance; J. Wilms et al. 2000) model to account for the interstellar absorption. The model-fitted unfolded spectrum is given in the Appendix in Figure 15. Although the χ^2/DOF value was acceptable, we noticed that the spectrum changes its slope above ~ 20 keV. Thus, we replaced the power-law with the broken-power-law model,¹³ which accounts for the change in slope after a certain energy, called the break energy (E_b). We call this model Model-1. The three distinct instruments (LE, ME, and HE) are normalized using the `constant`. Although this model fit was acceptable, there was a reflective nature in the spectrum. To account for that, we replaced the broken-power-law model with the reflection model in neutral medium `pexrav`¹⁴ (Model-2). With this Model-2, we also achieved the best-fit statistics. Then we checked the reflection component by using the reflection model `pexriv` (Model-3), which takes ionization into account. Using the Model-3, as mentioned before, we achieved the best-fit statistics. Here, we like to point out our approach using the Model-3. Except for 2 parameters, all the parameters of this model are the same as the `pexrav` model. While fitting with this model, we set the cutoff energy value to the one obtained from the fit with the `pexrav` model. Also, we found while fitting that the disk temperature parameter (in units of Kelvin) was always pegging to the highest value of 10^6 K. Thus, for all the spectral fitting using this model, we freeze the value of this parameter to the highest value. The extra parameter that this model has over `pexrav` is the disk ionization parameter (ξ), which is given as $\xi = 4\pi F_{\text{ion}}/n$, where n is the density of the reflector (C. Done et al. 1992) and F_{ion} is the irradiating flux in the 5 eV–20 keV energy band. For the analysis with Model-2 and Model-3, we fixed the abundances to solar abundance and also varied the value of the inclination to a narrow range of around 30° as reported by S. Mondal et al. (2024).

For all the fitting processes mentioned so far, the results are achieved by keeping the N_{H} free and varying in a broad range. Therefore, we take the average of N_{H} from all three models, which is $\sim 5.6 \times 10^{22} \text{ cm}^{-2}$. Then we reanalyzed all the observations using the same models (Model-1 to Model-3) combinations by keeping N_{H} fixed to the average value. The parameters of the fit do not change significantly by keeping N_{H} fixed to the average value. We report both the results by

¹⁰ <https://heasarc.gsfc.nasa.gov/xanadu/xspec/manual/node166.html>

¹¹ <https://heasarc.gsfc.nasa.gov/xanadu/xspec/manual/node221.html>

¹² <https://heasarc.gsfc.nasa.gov/xanadu/xspec/manual/node273.html>

¹³ <https://heasarc.gsfc.nasa.gov/xanadu/xspec/manual/node141.html>

¹⁴ <https://heasarc.gsfc.nasa.gov/xanadu/xspec/manual/node214.html>

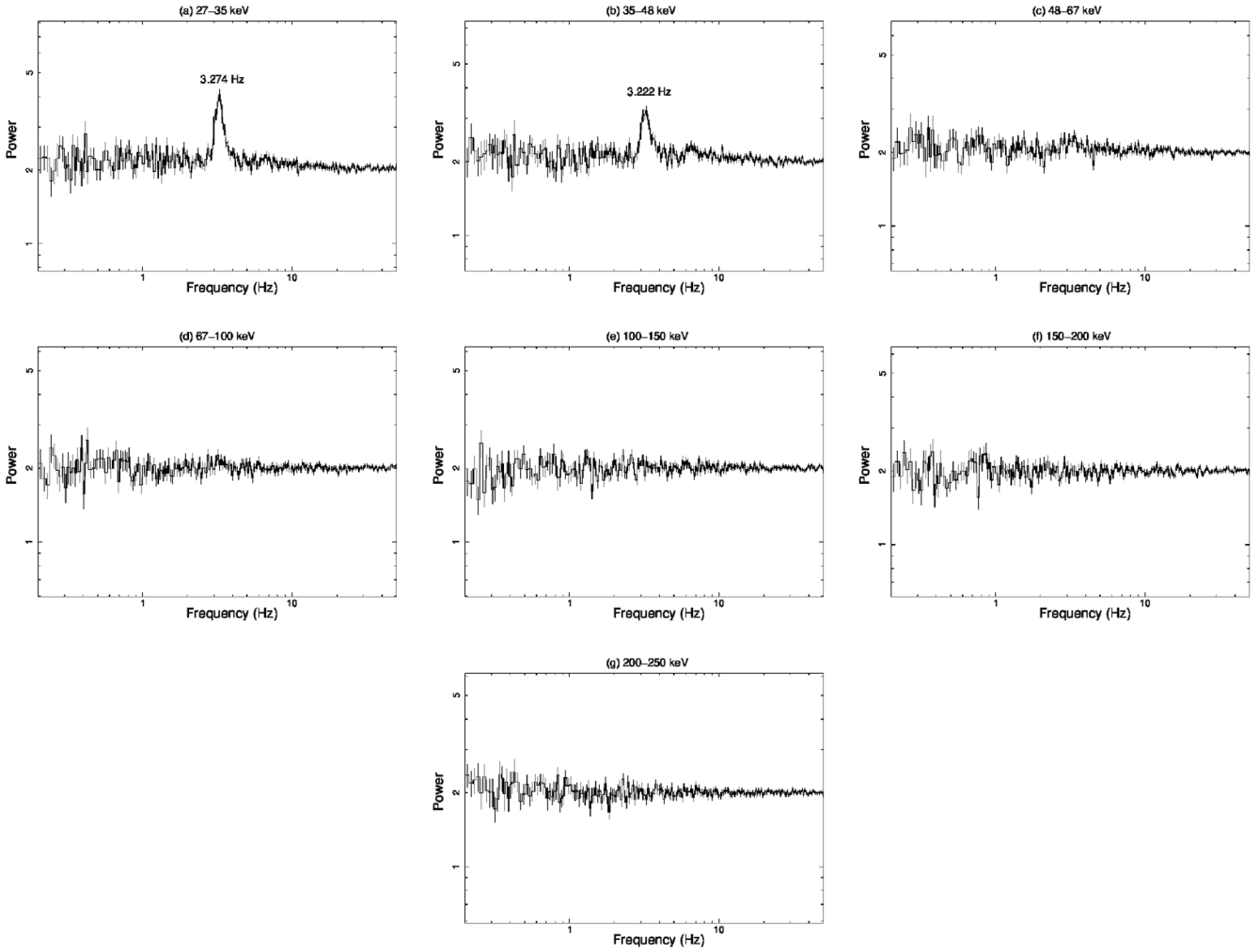


Figure 7. Energy-dependent PDS, produced in (a) 27–35, (b) 35–48, (c) 48–67, (d) 67–100, (e) 100–150, (f) 150–200, and (g) 200–250 keV energy bands using 0.01 s time-binned HE light curves. This is for the observation ID P0614374001 (exposure ID: P061437400101-20240304-01-0).

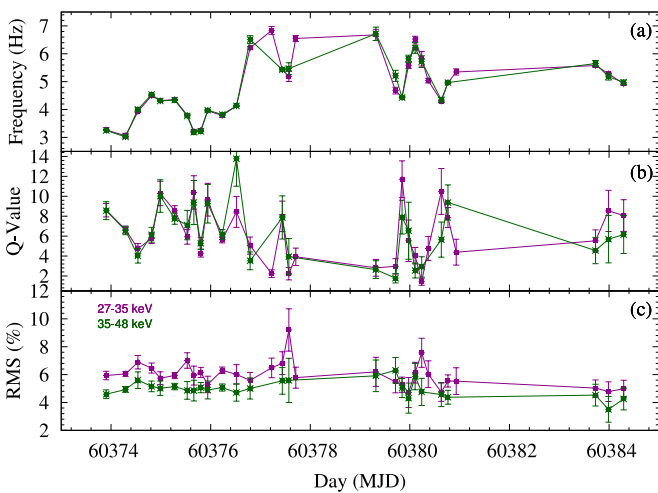


Figure 8. Variation in the energy-dependent (a) QPO frequency (in Hz), (b) Q-factor, and (c) rms (%) with time. Here, the magenta-colored points represent the values for 27–35 keV, whereas the green-colored points represent the values for 35–48 keV energy bands, respectively.

keeping N_{H} fixed and free in the next paragraph. All the best-fitted model parameters and statistics are given in Tables 5–10.

Since none of these models takes relativistic effects into account, we performed the same spectral analysis using the relativistic reflection model, `relxill`¹⁵, to see the relativistic effects. We consider this as Model-4, as mentioned before. For this model fitting, we used the average N_{H} value and froze it to $5.6 \times 10^{22} \text{ cm}^{-2}$ for all observations. The `relxill` model has a total of 14 parameters, of which several can be fixed to reasonable values in order to avoid degeneracy in the best-fit parameters (S. Mondal et al. 2024; J.-Q. Peng et al. 2024). From this model fitting, we can get some valuable information about the source, like its spin and disk inclination. To achieve the best fit with Model-4, we fixed some of the model parameters. We fixed $R_{\text{in}}=1$ and $R_{\text{out}}=1000$, $\text{index1}=\text{index2}=3$, $R_{\text{br}}=15$. For being a Galactic source, the redshift (z) was always kept to 0. The best-fitted parameters and statistics for this model fitting are listed in Table 11. In Figures 12(a)–(d), we show the model-fitted unfolded spectra using (a) Model-1, (b) Model-2, (c) Model-3, and (d) Model-4.

In Figure 13, we show the variations in some of the spectral parameters for all four models. In the top figure, we show the variations in the parameters when the N_{H} was free, whereas in

¹⁵ <https://www.sternwarte.uni-erlangen.de/%E2%88%BCdauser/research/relxill/>

Table 4
Results of Timing Analysis from Energy-dependent HE Light Curves

Time (MJD) (1)	27–35 keV				35–48 keV			
	Frequency (Hz) (2)	Q -Value (3)	rms (%) (4)	Significance (5)	Frequency (Hz) (6)	Q -Value (7)	rms (%) (8)	Significance (9)
60373.90	3.27 ± 0.01	8.6 ± 0.7	5.9 ± 0.3	15.1	3.25 ± 0.01	8.6 ± 0.9	4.6 ± 0.3	11.8
60374.29	3.06 ± 0.09	6.6 ± 0.3	6.1 ± 0.2	24.7	3.02 ± 0.01	6.6 ± 0.4	4.9 ± 0.2	19.2
60374.54	3.93 ± 0.03	4.7 ± 0.5	6.9 ± 0.5	11.3	4.01 ± 0.06	4.1 ± 0.7	5.6 ± 0.6	8.8
60374.81	4.50 ± 0.02	5.8 ± 0.5	6.5 ± 0.4	15.1	4.54 ± 0.03	6.1 ± 0.7	5.2 ± 0.4	11.8
60374.98	4.32 ± 0.01	10.2 ± 1.2	5.7 ± 0.4	9.4	4.31 ± 0.02	10.0 ± 1.6	5.0 ± 0.5	8.0
60375.27	4.36 ± 0.01	8.5 ± 0.5	5.9 ± 0.2	22.1	4.34 ± 0.01	7.8 ± 0.6	5.1 ± 0.2	18.2
60375.52	3.80 ± 0.02	5.9 ± 0.7	7.1 ± 0.6	10.2	3.77 ± 0.04	7.1 ± 1.5	4.9 ± 0.6	6.4
60375.66	3.22 ± 0.02	$10. \pm 1.7$	5.9 ± 0.7	6.1	3.19 ± 0.03	9.4 ± 2.2	4.8 ± 0.7	5.1
60375.80	3.26 ± 0.02	4.3 ± 0.4	6.2 ± 0.4	13.5	3.22 ± 0.02	5.3 ± 0.6	5.1 ± 0.4	11.4
60375.94	3.96 ± 0.02	9.6 ± 1.6	5.3 ± 0.6	7.0	3.98 ± 0.03	9.2 ± 1.9	4.9 ± 0.6	6.3
60376.23	3.79 ± 0.01	5.6 ± 0.3	6.3 ± 0.2	23.8	3.82 ± 0.01	6.2 ± 0.5	5.1 ± 0.2	16.6
60376.51	4.13 ± 0.03	8.4 ± 1.5	6.1 ± 0.7	6.8	4.13 ± 0.02	13.7 ± 2.8	4.7 ± 0.6	5.8
60376.79	6.21 ± 0.06	5.0 ± 0.9	5.6 ± 0.6	9.0	6.51 ± 0.14	3.5 ± 0.9	5.1 ± 0.8	6.0
60377.22	6.84 ± 0.14	2.2 ± 0.4	6.5 ± 0.7	7.7
60377.43	5.43 ± 0.04	7.9 ± 1.5	6.8 ± 0.8	6.9	5.43 ± 0.06	7.9 ± 2.2	5.5 ± 0.9	4.8
60377.56	5.19 ± 0.18	2.2 ± 0.6	9.2 ± 1.5	5.7	5.47 ± 0.21	3.9 ± 1.8	5.6 ± 1.5	3.0
60377.70	6.55 ± 0.11	3.9 ± 0.9	5.8 ± 0.8	7.2
60379.31	6.68 ± 0.20	2.8 ± 0.8	6.2 ± 1.1	6.5	6.72 ± 0.24	2.6 ± 0.9	5.9 ± 1.1	5.5
60379.71	4.68 ± 0.12	2.9 ± 0.8	5.5 ± 0.8	8.8	5.21 ± 0.20	1.8 ± 0.5	6.3 ± 0.9	8.3
60379.84	4.45 ± 0.02	$11. \pm 1.8$	5.3 ± 0.5	7.4	4.43 ± 0.04	7.9 ± 1.7	5.0 ± 0.7	5.9
60379.97	5.59 ± 0.12	5.5 ± 2.1	4.7 ± 1.1	3.9	5.82 ± 0.13	6.5 ± 2.9	4.3 ± 1.0	4.1
60380.10	6.53 ± 0.10	4.0 ± 0.8	6.1 ± 0.7	7.6	6.21 ± 0.19	2.5 ± 0.8	5.9 ± 0.9	7.7
60380.23	5.82 ± 0.26	1.4 ± 0.4	7.6 ± 1.1	7.7	5.72 ± 0.21	2.9 ± 1.1	4.8 ± 0.9	4.8
60380.36	5.04 ± 0.08	4.8 ± 1.2	6.1 ± 0.9	5.3
60380.63	4.30 ± 0.03	10.4 ± 2.3	4.7 ± 0.6	5.8	4.35 ± 0.08	5.6 ± 1.8	4.6 ± 0.9	4.7
60380.76	4.96 ± 0.03	7.9 ± 1.1	5.5 ± 0.4	10.6	4.97 ± 0.03	9.4 ± 1.8	4.4 ± 0.5	7.9
60380.93	5.35 ± 0.11	4.4 ± 1.3	5.5 ± 0.9	5.5
60383.72	5.58 ± 0.07	5.5 ± 1.1	5.1 ± 0.6	8.2	5.65 ± 0.11	4.6 ± 1.3	4.5 ± 0.8	5.4
60383.98	5.29 ± 0.05	8.5 ± 2.1	4.8 ± 0.7	6.0	5.18 ± 0.12	5.7 ± 2.4	3.5 ± 0.9	3.1
60384.29	4.92 ± 0.04	8.1 ± 1.6	4.9 ± 0.6	6.9	4.98 ± 0.08	6.1 ± 1.9	4.2 ± 0.8	4.8

Note. In column (1), we have listed the MJDs of the exposure IDs we used. Columns (2), (3), (4), and (5) represent the QPO frequency (in Hz), Q -value, rms (%), and significance in the 27–35 keV energy band. Columns (6), (7), (8), and (9) represent the QPO frequency (in Hz), Q -value, rms (%), and significance in the 35–48 keV energy band.

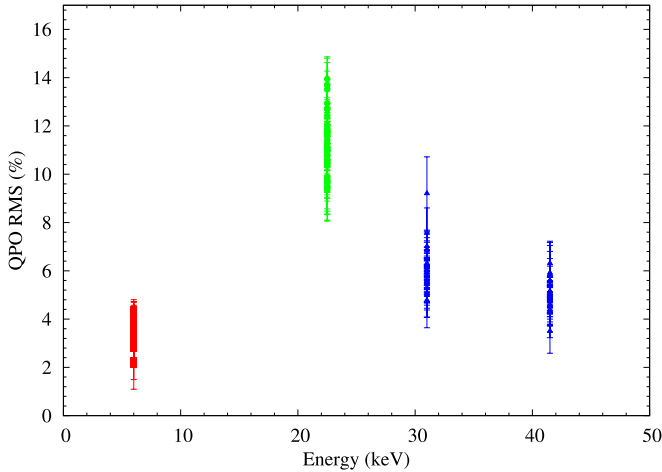


Figure 9. Variation in the QPO rms with energy. The red, green, and blue points represent data points using LE, ME, and HE bands light curves, respectively, for all the exposures.

the bottom figure, we show the variations in the same parameters when N_{H} was fixed to an average value. In panel (a), we show the variations in N_{H} for three different models (red filled square for Model-1, blue filled square for Model-2,

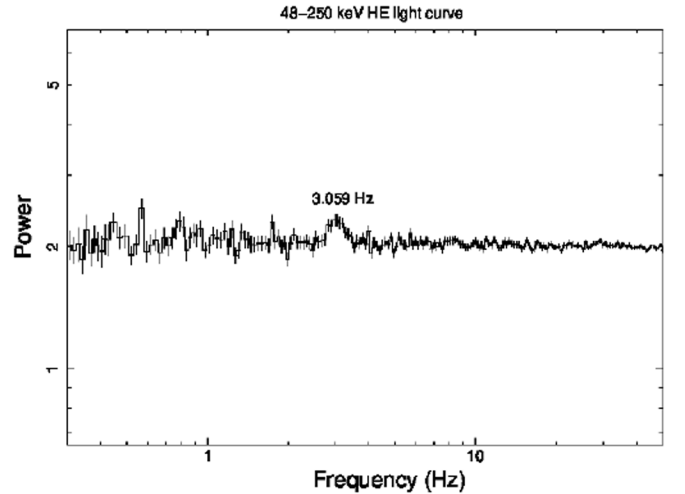


Figure 10. PDS in the 48–250 keV energy band for the HE light curve of the exposure ID. P061437400103-20240305-02-01.

and green filled square for Model-3). We notice that they show consistent variations within the error range throughout. The N_{H} for Model-1 varies between $(4.3 \text{ and } 6.5) \times 10^{22} \text{ cm}^{-2}$, $(5.1\text{--}6.3) \times 10^{22} \text{ cm}^{-2}$ for Model-2 and $(5\text{--}6.9) \times 10^{22}$ for

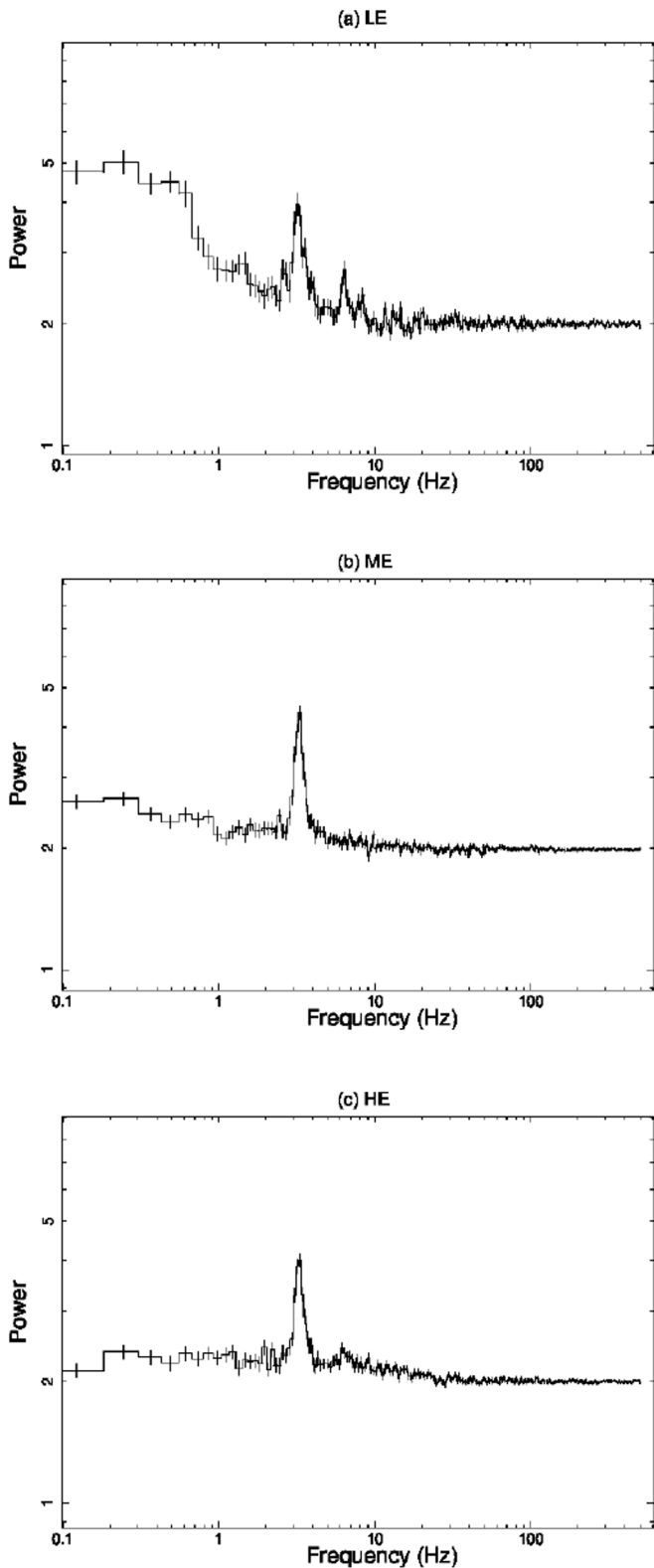


Figure 11. PDS continuum in the 0.1–500 Hz frequency range for (a) LE, (b) ME, and (c) HE bands. This is for the observation ID P0614374001 (exposure ID: P061437400101-20240304-01-0).

Model-3. In panel (d), we show the variations in the inner-disk temperature (T_{in} in keV) for all four models for a fixed N_{H} . The T_{in} shows variation in the range of 0.9–1.9 keV for all four models. In panel (e), we show the variations in the photon indices. The red filled squares and empty squares represent Γ

and Γ_2 for the broken-power-law model, where the blue, green, and black filled squares represent the Γ of the pexrav, pexriv, and relxill models. We notice that the photon index was high if we take the presence of type-C QPOs into consideration. We also note that both the T_{in} and $\text{Norm}_{\text{diskbb}}$ values did not show typical variations as was observed for other BHCs (R. A. Remillard & J. E. McClintock 2006). When an outburst progresses, the normalization generally decreases from a high value. In this case, we have not seen that trend; rather, it varied randomly. In general, T_{in} increases as an outburst progresses, reflecting the movement of the disk inward. Here, for all the model combinations, we did not notice that increasing the profile. The pexriv model-fitted ionization parameter is low here in the range of 2.4×10^{-13} – 3.8×10^{-8} , the reason for which is not clear. Since the ionization parameter is low, the estimated irradiation flux (F_{ion}) is also very low, which can be estimated using the relation $\xi = 4\pi F_{\text{ion}}/n$, where n is the density of the reflector (C. Done et al. 1992) and F_{ion} is the irradiating flux in the 5 eV–20 keV energy band.

The relxill model fits provided a broad range for both the spin and inclination parameters of the source to be 0.5–0.81 and 10–41 (in degrees). This could also be due to the degeneracy in model parameters and significant changes in $\text{Norm}_{\text{diskbb}}$. In particular, on the last exposure ID, we found that the $\text{Norm}_{\text{diskbb}}$ increased to a very high value, compared to other IDs, and the disk temperature decreased to 0.9, whereas the photon index increased to 3.3. However, the ranges of the spin and inclination parameters cover the estimations in S. Mondal et al. (2024). Since the last exposure ID returned a very high photon index, we conclude the spectral state as SS, as was reported earlier by S. Mondal et al. (2024). The absence of QPO also supports the same spectral state. We found that the ionization parameter in the relxill model fitting was high (>3) and the iron abundance (A_{Fe}) varied from 1.1 to 4.9. The reflection fraction varied in a range of 0.12–2.29. The E_{cut} also showed random variations. We discuss the possible reasons in the next section.

3.3. Evolution of the Shock

In the TCAF scenario, the oscillation of the shock produces QPOs. According to this model, the QPO frequency can be written as (D. Molteni et al. 1996; S. K. Chakrabarti et al. 2005),

$$\nu_{\text{qpo}} = \frac{c^3}{2GM_{\text{BH}}} \frac{1}{RX_s(X_s - 1)^{1/2}} \text{ Hz}, \quad (1)$$

where the following are represented, respectively: c , G , M_{BH} , X_s , and R ; these are the speed of light, the gravitational constant, the mass of the BH, the shock location, and the ratio of matter densities in postshock to preshock regions (ρ_+/ρ_-).

The QPO frequencies (ν_{qpo}) are estimated from timing analysis as discussed earlier, and the shock locations during the outburst are estimated using the above relation in Equation (1). We found that at the beginning of the outburst, the shock was located at a distance of $\sim 100 r_s$ from the BH (see Figure 14(b)). Later, as the ν_{qpo} increased, the shock moved inward, decreasing the size of the corona. After a few days, the shock became stable. Table 3 provides the values for the shock locations (columns (11)–(13)).

Table 5
Properties from Spectral Analysis Using Model-1

Time MJD (1)	TBabs N_{H} (2)	diskbb		Broken Power Law				Fitting Constants		Fitting Stat χ^2/DOF (11)
		T_{in} (keV) (3)	Norm (4)	Γ_1 (5)	E_b (keV) (6)	Γ_2 (7)	Norm (8)	Constant1 (9)	Constant2 (10)	
60373.90	5.1 ± 0.1	1.6 ± 0.3	145 ± 8	2.4 ± 0.2	19.2 ± 0.3	3.1 ± 0.2	15.4 ± 1.1	1.10 ± 0.01	1.15 ± 0.02	1242.96/1410
60374.98	5.1 ± 0.2	1.4 ± 0.1	278 ± 23	2.5 ± 0.4	15.1 ± 0.4	2.9 ± 0.2	19.8 ± 2.5	1.01 ± 0.01	0.97 ± 0.02	1238.56/1410
60375.94	4.9 ± 0.2	1.4 ± 0.1	222 ± 23	2.5 ± 0.4	14.4 ± 0.5	2.9 ± 0.2	18.5 ± 2.3	1.04 ± 0.01	1.04 ± 0.02	1188.51/1410
60376.96	4.3 ± 0.4	1.2 ± 0.1	844 ± 103	2.2 ± 0.2	10.7 ± 0.2	3.1 ± 0.2	7.2 ± 4.9	0.96 ± 0.02	0.91 ± 0.03	1186.14/1410
60377.98	4.7 ± 0.3	1.2 ± 0.1	755 ± 75	2.4 ± 0.2	11.4 ± 0.2	3.3 ± 0.2	11.8 ± 4.4	1.00 ± 0.02	0.89 ± 0.04	1204.31/1410
60378.83	4.7 ± 0.2	1.2 ± 0.1	590 ± 61	2.4 ± 0.1	11.0 ± 0.2	3.2 ± 0.2	14.2 ± 3.4	0.95 ± 0.01	1.06 ± 0.03	1266.20/1410
60379.84	5.4 ± 0.1	1.4 ± 0.3	136 ± 20	2.8 ± 0.3	14.5 ± 0.8	3.1 ± 0.2	27.9 ± 2.0	1.01 ± 0.01	1.15 ± 0.03	1234.25/1410
60380.93	5.4 ± 0.1	1.4 ± 0.3	129 ± 20	2.8 ± 0.3	14.2 ± 1.1	2.9 ± 0.2	27.9 ± 2.0	1.03 ± 0.01	0.96 ± 0.03	1184.85/1410
60381.75	5.5 ± 0.2	1.2 ± 0.2	339 ± 49	2.8 ± 0.5	11.8 ± 0.1	3.8 ± 0.3	27.5 ± 3.4	0.96 ± 0.01	0.93 ± 0.04	1270.61/1410
60382.93	5.6 ± 0.2	1.4 ± 0.3	102 ± 34	2.7 ± 0.5	12.0 ± 0.3	3.5 ± 0.3	29.2 ± 3.2	0.94 ± 0.01	1.06 ± 0.04	1243.06/1410
60383.85	5.0 ± 0.2	1.6 ± 0.3	69 ± 19	2.7 ± 0.5	13.1 ± 0.7	3.2 ± 0.3	21.0 ± 2.4	0.99 ± 0.02	1.32 ± 0.09	1299.35/1410
60383.98	5.2 ± 0.2	1.4 ± 0.3	80 ± 25	2.8 ± 0.5	13.2 ± 1.2	3.1 ± 0.3	23.2 ± 2.6	1.02 ± 0.02	1.03 ± 0.03	1312.79/1410
60384.12	5.2 ± 0.1	1.4 ± 0.2	75 ± 18	2.8 ± 0.3	14.4 ± 1.6	2.9 ± 0.3	21.9 ± 1.8	1.04 ± 0.02	0.99 ± 0.03	1188.29/1410
60386.59	6.4 ± 0.3	0.9 ± 0.2	758 ± 117	3.5 ± 0.9	8.5 ± 0.3	2.8 ± 0.2	34.5 ± 6.8	1.05 ± 0.02	1.07 ± 0.05	1344.08/1410

Note. Column (1) represents the MJD of those respective Exposure IDs for which we have performed spectral analysis. Column (2) gives the values of the hydrogen column densities (N_{H}) of those analyzed exposures. Columns (3) and (4) give the values of the parameters from the diskbb model. Columns (5)–(8) give the values of the parameters from the broken-power-law model. Columns (9) and (10) give the values of the constants needed to achieve simultaneous broadband fitting. Column (11) gives the values of the χ^2/DOF for each fitting. The errors are estimated with a 90% confidence interval, which corresponds to 1.645σ in XSPEC.

Table 6
Properties from Spectral Analysis Using Model-1 by Freezing the Column Density (N_{H}) to $5.6 \times 10^{22} \text{ cm}^{-2}$.

Time MJD (1)	diskbb		Broken Power Law				Fitting Constants		Fitting Stat χ^2/DOF (10)
	T_{in} (keV) (2)	Norm (3)	Γ (4)	E_b (keV) (5)	Γ (6)	Norm (7)	Constant1 (8)	Constant2 (9)	
60373.90	1.6 ± 0.1	116 ± 7	2.6 ± 0.3	20.5 ± 1.2	3.1 ± 0.2	20.6 ± 1.2	1.08 ± 0.02	1.14 ± 0.02	1261.70/1411
60374.98	1.4 ± 0.1	221 ± 27	2.6 ± 0.4	16.1 ± 0.8	2.9 ± 0.1	27.6 ± 2.3	1.00 ± 0.02	0.97 ± 0.02	1246.82/1411
60375.94	1.4 ± 0.2	141 ± 25	2.7 ± 0.4	16.4 ± 0.6	2.9 ± 0.3	28.8 ± 3.2	1.04 ± 0.03	1.07 ± 0.02	1204.47/1411
60376.96	1.2 ± 0.1	581 ± 93	2.7 ± 0.2	6.9 ± 0.5	3.1 ± 0.4	28.9 ± 3.9	1.05 ± 0.02	1.01 ± 0.03	1211.79/1328
60377.98	1.2 ± 0.3	537 ± 68	2.8 ± 0.2	12.0 ± 0.7	3.3 ± 0.4	28.3 ± 3.4	1.03 ± 0.02	0.92 ± 0.02	1210.63/1411
60378.83	1.3 ± 0.1	357 ± 45	2.8 ± 0.2	11.5 ± 0.5	3.2 ± 0.2	30.7 ± 3.3	0.98 ± 0.02	1.09 ± 0.02	1283.22/1411
60379.84	1.4 ± 0.2	110 ± 15	2.8 ± 0.3	15.2 ± 1.2	3.0 ± 0.2	31.1 ± 2.3	1.02 ± 0.04	1.16 ± 0.02	1236.82/1411
60380.93	1.4 ± 0.1	109 ± 17	2.8 ± 0.4	14.9 ± 1.2	2.9 ± 0.2	30.3 ± 3.0	1.03 ± 0.02	0.96 ± 0.02	1186.33/1411
60381.75	1.2 ± 0.2	320 ± 27	2.8 ± 0.4	11.9 ± 1.1	3.8 ± 0.2	28.9 ± 3.2	0.96 ± 0.02	0.93 ± 0.04	1270.78/1411
60382.93	1.4 ± 0.2	103 ± 37	2.7 ± 0.3	12.1 ± 1.2	3.5 ± 0.2	29.1 ± 3.1	0.94 ± 0.02	1.06 ± 0.02	1243.06/1411
60383.85	1.8 ± 0.1	30 ± 6	2.8 ± 0.2	14.9 ± 0.5	3.1 ± 0.2	28.9 ± 2.6	1.00 ± 0.03	1.33 ± 0.02	1310.91/1411
60383.98	1.5 ± 0.1	48 ± 7	2.8 ± 0.4	14.1 ± 1.1	3.0 ± 0.2	27.8 ± 2.5	1.02 ± 0.02	1.03 ± 0.02	1317.29/1411
60384.12	1.5 ± 0.2	40 ± 8	2.8 ± 0.3	15.4 ± 1.3	2.9 ± 0.2	27.3 ± 1.9	1.03 ± 0.02	0.98 ± 0.03	1201.22/1411
60386.59	0.9 ± 0.2	1029 ± 108	3.3 ± 0.8	8.6 ± 0.6	2.8 ± 0.3	17.6 ± 5.9	1.06 ± 0.02	1.06 ± 0.05	1355.04/1411

Note. Column (1) represents the MJD of those respective Exposure IDs for which we have performed spectral analysis. Columns (2) and (3) give the values of the parameters from the diskbb model. Columns (4)–(7) give the values of the parameters from the broken-power-law model. Columns (8) and (9) give the values of the constants needed to achieve simultaneous broadband fitting. Column (10) gives the values of the χ^2/DOF for each fitting. The errors are estimated with a 90% confidence interval, which corresponds to 1.645σ in XSPEC.

Table 7
Properties from Spectral Analysis Using Model-2

Time MJD (1)	TBabs N_{H} (2)	diskbb		pexrav				Fitting Constants		Fitting Stat χ^2/DOF (11)
		T_{in} (keV) (3)	Norm (4)	Γ (5)	E_{cut} (6)	rel _{frac} (7)	Norm (8)	Constant1 (9)	Constant2 (10)	
60373.90	5.7 ± 0.2	1.6 ± 0.3	98 ± 2	2.6 ± 0.1	82 ± 3	0.32 ± 0.01	22.9 ± 2.4	1.07 ± 0.01	1.07 ± 0.02	1554.44/1409
60374.98	5.8 ± 0.2	1.4 ± 0.1	198 ± 5	2.6 ± 0.1	82 ± 1	0.01 ± 0.01	30.1 ± 2.6	0.98 ± 0.02	0.98 ± 0.02	1451.32/1409
60375.94	5.6 ± 0.3	1.5 ± 0.1	130 ± 3	2.6 ± 0.1	76 ± 1	0.05 ± 0.01	28.6 ± 2.6	1.04 ± 0.02	1.08 ± 0.03	1397.76/1409
60376.96	5.1 ± 0.4	1.3 ± 0.3	477 ± 8	2.6 ± 0.1	45 ± 2	0.10 ± 0.01	22.2 ± 2.6	1.09 ± 0.03	1.17 ± 0.05	1522.15/1409
60377.98	5.9 ± 0.4	1.3 ± 0.2	404 ± 8	2.8 ± 0.1	42 ± 3	0.05 ± 0.01	35.6 ± 2.4	1.07 ± 0.02	1.10 ± 0.08	1400.06/1409
60378.83	6.2 ± 0.3	1.4 ± 0.2	166 ± 5	2.9 ± 0.1	106 ± 4	0.05 ± 0.01	46.9 ± 2.4	1.04 ± 0.01	1.15 ± 0.04	1620.60/1409
60379.84	5.8 ± 0.2	1.5 ± 0.2	74 ± 3	2.9 ± 0.1	179 ± 2	0.14 ± 0.01	35.9 ± 2.4	1.03 ± 0.02	1.17 ± 0.04	1474.45/1409
60380.93	5.6 ± 0.1	1.4 ± 0.3	100 ± 4	2.8 ± 0.1	124 ± 2	0.05 ± 0.01	30.6 ± 2.8	1.04 ± 0.02	1.00 ± 0.04	1409.79/1409
60381.75	6.1 ± 0.1	1.4 ± 0.3	120 ± 3	2.7 ± 0.1	16 ± 1	0.05 ± 0.01	35.9 ± 2.8	1.04 ± 0.02	1.33 ± 0.07	1632.36/1409
60382.93	6.3 ± 0.2	2.1 ± 0.2	16 ± 1	2.9 ± 0.2	53 ± 2	0.05 ± 0.01	42.6 ± 2.8	0.99 ± 0.01	1.13 ± 0.06	1431.01/1409
60383.85	5.4 ± 0.3	1.8 ± 0.2	31 ± 1	2.7 ± 0.1	44 ± 1	0.15 ± 0.01	25.3 ± 2.8	1.01 ± 0.02	1.48 ± 0.05	1433.76/1409
60383.98	5.7 ± 0.2	1.6 ± 0.2	36 ± 2	2.9 ± 0.1	211 ± 2	0.05 ± 0.01	29.2 ± 2.8	1.04 ± 0.02	1.03 ± 0.04	1440.43/1409
60384.12	5.5 ± 0.2	1.6 ± 0.2	41 ± 2	2.9 ± 0.1	373 ± 5	0.11 ± 0.01	27.2 ± 2.8	1.05 ± 0.01	1.02 ± 0.04	1321.88/1409
60386.59	5.7 ± 0.1	0.9 ± 0.1	1320 ± 72	3.3 ± 0.2	374	1.95 ± 0.19	18.5 ± 1.9	1.05 ± 0.02	1.64 ± 0.11	1420.99/1410

Note. Column (1) represents the MJD of those respective Exposure IDs for which we have performed spectral analysis. Column (2) gives the values of hydrogen column densities (N_{H}) of those analyzed exposures. Columns (3) and (4) give the values of the parameters from the diskbb model. Columns (5)–(8) give the values of the parameters from the pexrav model. Columns (9) and (10) give the values of the constants needed to achieve simultaneous broadband fitting. Column (11) gives the values of the χ^2/DOF for each fitting. The errors are estimated with a 90% confidence interval, which corresponds to 1.645σ in XSPEC.

4. Discussions

The Galactic BH Swift J151857.0-572147 started an outburst recently in 2024 March. We have used Insight-HXMT data for both our timing and spectral studies from 2024 March 4 to 2024 March 17. Using the 0.01 s time-binned light curves from the three instruments of HXMT (LE, ME, and HE), we studied the source’s timing properties. We also searched for the energy dependence of LFQPOs by producing light curves in seven different energy ranges within the HE band. Along with these, we searched for HFQPOs in all the PDS from LE, ME, and HE using 1 ms time-binned light

curves. We then examined the combined LE+ME+HE spectra in the 2–100 keV broad energy band to learn more about the spectral characteristics of this source using the spectra files from these three instruments.

For stellar-mass BHs, QPOs are one of the most significant and frequent occurrences. We examined 186 exposures in total for this recently found source (62 for each of LE, ME, and HE). Nevertheless, incorrect light curve production occurred in two LE exposures. A total of 184 light curves for LE, ME, and HE were obtained. The details are listed in Table 2. We discovered that QPO was not present in each of these light curves. The details on QPO properties are listed in Table 3.

Table 8
Properties from Spectral Analysis Using Model-2 by Freezing the Column Density (N_{H}) to $5.6 \times 10^{22} \text{ cm}^{-2}$.

Time MJD (1)	diskbb		pexrav				Fitting Constants		Fitting Stat χ^2/DOF (10)
	T_{in} (keV) (2)	Norm (3)	Γ (4)	E_{cut} (5)	rel_{frac} (6)	Norm (7)	Constant1 (8)	Constant2 (9)	
60373.90	1.6 ± 0.2	109 ± 2	2.5 ± 0.1	70 ± 3	0.22 ± 0.01	20.7 ± 2.2	1.07 ± 0.01	1.06 ± 0.04	1555.59/1410
60374.98	1.4 ± 0.2	212 ± 4	2.6 ± 0.1	73 ± 4	0.05 ± 0.01	27.3 ± 2.4	0.99 ± 0.02	0.98 ± 0.03	1453.48/1410
60375.94	1.5 ± 0.3	130 ± 4	2.6 ± 0.1	76 ± 4	0.05 ± 0.01	28.5 ± 2.4	1.04 ± 0.04	1.08 ± 0.02	1397.81/1410
60376.96	1.4 ± 0.4	563 ± 18	2.6 ± 0.1	35 ± 2	0.10 ± 0.01	25.8 ± 2.1	1.05 ± 0.03	1.26 ± 0.04	1594.50/1410
60377.98	1.4 ± 0.4	457 ± 12	2.7 ± 0.1	33 ± 3	0.05 ± 0.01	28.7 ± 2.1	1.07 ± 0.02	1.14 ± 0.06	1403.88/1410
60378.83	1.4 ± 0.3	241 ± 9	2.8 ± 0.1	53 ± 4	0.05 ± 0.01	33.1 ± 2.3	1.05 ± 0.01	1.23 ± 0.02	1657.64/1410
60379.84	1.4 ± 0.2	98 ± 3	2.8 ± 0.1	117 ± 9	0.05 ± 0.01	31.1 ± 1.9	1.03 ± 0.02	1.16 ± 0.05	1477.93/1410
60380.93	1.4 ± 0.1	102 ± 3	2.8 ± 0.1	123 ± 8	0.05 ± 0.01	30.2 ± 2.7	1.04 ± 0.03	1.00 ± 0.03	1409.89/1410
60381.75	1.3 ± 0.1	200 ± 3	2.5 ± 0.1	13 ± 1	0.05 ± 0.01	27.7 ± 2.4	1.03 ± 0.02	1.42 ± 0.06	1641.72/1410
60382.93	1.7 ± 0.2	42 ± 3	2.7 ± 0.2	26 ± 2	0.05 ± 0.01	29.8 ± 2.3	1.01 ± 0.01	1.31 ± 0.03	1470.61/1410
60383.85	1.9 ± 0.3	24 ± 1	2.8 ± 0.1	60 ± 3	0.25 ± 0.01	29.2 ± 2.3	1.01 ± 0.02	1.45 ± 0.04	1434.88/1410
60383.98	1.6 ± 0.2	39 ± 2	2.8 ± 0.1	197 ± 4	0.06 ± 0.01	28.4 ± 2.1	1.05 ± 0.02	1.03 ± 0.03	1440.85/1410
60384.12	1.6 ± 0.2	37 ± 2	2.9 ± 0.1	529 ± 6	0.22 ± 0.01	28.3 ± 1.8	1.05 ± 0.02	1.02 ± 0.06	1322.09/1410
60386.59	0.9 ± 0.1	1305 ± 97	3.3 ± 0.2	373	1.68 ± 0.15	16.3 ± 3.9	1.04 ± 0.06	1.54 ± 0.09	1419.64/1411

Note. Column (1) represents the MJD of those respective Exposure IDs for which we have performed spectral analysis. Columns (2) and (3) give the values of the parameters from the diskbb model. Columns (4)–(7) give the values of the parameters from the pexrav model. Columns (8) and (9) give the values of the constants needed to achieve simultaneous broadband fitting. Column (10) gives the values of the χ^2/DOF for each fitting. The errors are estimated with a 90% confidence interval, which corresponds to 1.645σ in XSPEC.

Over the analysis period of ~ 13 days, the QPO frequency has rapidly changed. In our analysis period, the ν_{qpo} showed variation approximately from 3.3 to 7.4, 3.2 to 9, and 3.2 to 7 Hz in LE, ME, and HE bands, respectively. Even in a single day, there was a change in the QPO frequency (ν_{qpo}). The results section contains a general discussion on the evolution of QPO frequencies. Type-C QPO nature is identified from the fluctuation of QPO frequency, (%rms), and Q -factor. One thing we would like to discuss here is that the difference in rms value (in Table 3) for LE, ME, and HE is due to the large variation in background counts in these three bands. As we can notice in Table 2, the background count in the HE band is almost equivalent to the source count in the HE band for this source. The high background count rate in the HE band could be due to the contribution of the close proximity of the other source, Cir X-1, and the high effective area of the detector in this band. However, it was previously reported by J.-Q. Peng et al. (2024) that Cir X-1 was mainly present in the soft spectral state during the outburst of Swift J151857.0-572147. Thus, it could only have contributed to the LE band. Thereby, the reason for this high background rate cannot be firmly concluded.

Even though the QPOs have been thoroughly examined in the literature using observations from other sources, further modeling is necessary to understand their origin and connection with the spectral properties. Here, we want to concentrate on the physical scenario that explains how shock instabilities in advective flows near BHs give rise to QPOs. It is already explained in the introduction how the shock oscillations in the TCAF model explain the origin of the QPOs. This shock may not be stable at the outer edge over time. There could be oscillations in the CENBOL boundary, which can be caused due to either of two reasons:

(i) According to S. K. Chakrabarti (1989), the satisfaction of the Rankine–Hugoniot condition makes the boundary of the shock stable and steady. However, if this condition is not

satisfied (D. Ryu et al. 1997), the shock could oscillate at the outer boundary. It could produce variability in the light curves.

(ii) D. Molteni et al. (1996) stated that the presence of cooling may cause the shock to oscillate. QPOs emerge during the oscillation when the compressional heating timescale and the cooling timescale due to the inverse Comptonization process match (see S. K. Chakrabarti et al. 2015).

Depending on the flow parameters causing shocks, X_s can be anywhere over $10 r_s$. When the spectral nature of an outburst is hard, the shock forms far away $\sim 1000 r_s$, and it gradually becomes small in the following days as cooling increases (S. Mondal et al. 2015). For this outburst, the shock was far from the BH at the start of our analysis period. As the spectral nature of the outburst was softening, the shock moved inward, suggesting cooling was in progress. As the shock moved inward, the QPO frequency increased.

Although MAXI/GSC observed the source, it was not identified as a new source due to the proximity of another source, called Cir X-1. Thus, from the HXMT extracted light curves and HR variations, we may say that the source transitioned past its HS at the start of our analysis period and was already moved to the intermediate state. The variation in the photon index supports the above spectral state. At the start of our analysis period, the shock was at a distance, which suggests that the source had already completed its HS and was in the intermediate state. Later, the shock moved inward, suggesting the source is making a transition toward the SS. The nonidentification of type-B QPO does not help to designate a transition between the HIMS and SIMS, and thus, we consider this overall observation period to belong to the intermediate state. On several exposure IDs, we did not notice any QPO signature from the start of our analysis to the end in any of the three bands (Tables 2 and 3 for correspondence). This could be because of the mismatch of the heating and cooling timescales at the shock. For several exposure IDs, QPO is only present in one of the three bands, whereas for some of them, it was present in two bands (Tables 2 and 3 for

Table 9
Properties from Spectral Analysis Using Model-3

Time MJD (1)	TBabs N_{H} (2)	diskbb		pexriv				Fitting Constants		Fitting Stat χ^2/DOF (11)
		T_{in} (keV) (3)	Norm (4)	Γ (5)	rel_{frac} (6)	ξ (7)	Norm (8)	Constant1 (9)	Constant2 (10)	
60373.90	6.9 ± 0.2	1.5 ± 0.2	121 ± 2	2.6 ± 0.2	0.13 ± 0.02	9.2E-09	27.9 ± 2.2	1.06 ± 0.01	1.07 ± 0.02	1201.95/1409
60374.98	6.2 ± 0.2	1.4 ± 0.1	248 ± 4	2.6 ± 0.1	0.01 ± 0.01	4.4E-13	30.1 ± 2.4	1.00 ± 0.01	1.00 ± 0.03	1210.39/1409
60375.94	5.5 ± 0.3	1.5 ± 0.1	136 ± 3	2.6 ± 0.1	0.01 ± 0.01	1.6E-10	27.6 ± 2.4	1.05 ± 0.01	1.10 ± 0.03	1230.26/1409
60376.96	5.0 ± 0.3	1.3 ± 0.1	447 ± 8	2.6 ± 0.2	0.10 ± 0.01	1.0E-08	22.5 ± 2.4	1.07 ± 0.02	1.16 ± 0.05	1279.92/1409
60377.98	5.9 ± 0.4	1.3 ± 0.1	389 ± 8	2.8 ± 0.1	0.01 ± 0.01	2.4E-13	36.1 ± 2.2	1.06 ± 0.02	1.09 ± 0.07	1253.45/1409
60378.83	6.4 ± 0.3	1.5 ± 0.1	135 ± 5	3.0 ± 0.1	0.05 ± 0.01	2.9E-09	52.4 ± 2.2	1.03 ± 0.01	1.19 ± 0.04	1392.68/1409
60379.84	5.8 ± 0.2	1.5 ± 0.1	76 ± 4	2.9 ± 0.1	0.15 ± 0.05	1.6E-10	35.8 ± 2.2	1.03 ± 0.01	1.17 ± 0.03	1258.84/1409
60380.93	5.6 ± 0.1	1.4 ± 0.1	96 ± 3	2.8 ± 0.1	0.06 ± 0.01	6.6E-09	31.0 ± 2.6	1.04 ± 0.01	1.00 ± 0.04	1195.57/1409
60381.75	6.0 ± 0.1	1.4 ± 0.1	112 ± 2	2.7 ± 0.1	0.05 ± 0.01	5.8E-12	36.3 ± 2.5	1.03 ± 0.01	1.33 ± 0.06	1397.17/1409
60382.93	6.4 ± 0.2	2.1 ± 0.1	16 ± 1	2.9 ± 0.2	0.14 ± 0.01	1.5E-09	44.2 ± 2.5	0.99 ± 0.01	1.17 ± 0.06	1285.72/1409
60383.85	5.4 ± 0.3	1.8 ± 0.1	30 ± 1	2.7 ± 0.1	0.18 ± 0.01	2.6E-09	25.9 ± 2.6	1.01 ± 0.02	1.51 ± 0.15	1329.20/1409
60383.98	5.7 ± 0.2	1.7 ± 0.1	33 ± 2	2.9 ± 0.1	0.17 ± 0.01	2.2E-11	30.8 ± 2.6	1.04 ± 0.02	1.07 ± 0.04	1326.96/1409
60384.12	5.5 ± 0.2	1.6 ± 0.1	44 ± 2	2.9 ± 0.1	0.18 ± 0.01	6.5E-11	26.9 ± 2.6	1.05 ± 0.02	1.03 ± 0.03	1185.50/1409
60386.59	5.8 ± 0.2	0.9 ± 0.1	1437 ± 11	3.4 ± 0.4	2.24 ± 0.15	3.8E-08	18.4 ± 1.3	1.00 ± 0.02	1.64 ± 0.14	1277.63/1409

Note. Column (1) represents the MJD of those respective Exposure IDs for which we have performed spectral analysis. Column (2) gives the values of hydrogen column densities (N_{H}) of those analyzed exposures. Columns (3) and (4) give the values of the parameters from the diskbb model. Columns (5)–(8) give the values of the parameters from the pexriv model. Columns (9) and (10) give the values of the constants needed to achieve simultaneous broadband fitting. Column (11) gives the values of the χ^2/DOF for each fitting. For this model fitting, we have fixed the E_{cut} of this model to the E_{cut} of the pexrav model. Also, the disk temperature was set to 10^6 K. Since the ionization parameter ξ has such small value, we did not estimate the error for this parameter. The errors are estimated with a 90% confidence interval, which corresponds to 1.645σ in XSPEC.

Table 10
Properties from Spectral Analysis Using Model-3 by Freezing the Column Density (N_{H}) to $5.6 \times 10^{22} \text{ cm}^{-2}$

Time MJD (1)	diskbb		pexriv				Fitting Constants		Fitting Stat χ^2/DOF (10)
	T_{in} (keV) (2)	Norm (3)	Γ (4)	rel_{frac} (5)	ξ (6)	Norm (7)	Constant1 (8)	Constant2 (9)	
60373.90	1.6 ± 0.2	106 ± 2	2.6 ± 0.2	0.29 ± 0.02	1.3E-08	21.6 ± 2.2	1.08 ± 0.02	1.08 ± 0.02	1234.40/1410
60374.98	1.4 ± 0.2	207 ± 4	2.6 ± 0.4	0.05 ± 0.03	9.8E-17	27.9 ± 2.4	1.01 ± 0.01	1.01 ± 0.03	1218.89/1410
60375.94	1.5 ± 0.2	133 ± 3	2.6 ± 0.4	0.06 ± 0.01	2.4E-13	28.7 ± 2.4	1.05 ± 0.03	1.09 ± 0.01	1232.77/1410
60376.96	1.3 ± 0.2	443 ± 9	2.7 ± 0.3	0.10 ± 0.03	2.2E-12	30.7 ± 2.1	1.03 ± 0.02	1.20 ± 0.05	1286.38/1328
60377.98	1.3 ± 0.2	419 ± 7	2.8 ± 0.7	0.06 ± 0.01	3.4E-15	30.0 ± 2.1	1.08 ± 0.02	1.07 ± 0.05	1257.22/1410
60378.83	1.4 ± 0.2	220 ± 5	2.9 ± 0.4	0.05 ± 0.01	1.3E-17	35.1 ± 2.3	1.08 ± 0.01	1.12 ± 0.04	1438.47/1411
60379.84	1.5 ± 0.1	89 ± 3	2.8 ± 0.3	0.11 ± 0.04	1.5E-14	32.3 ± 2.9	1.04 ± 0.04	1.15 ± 0.03	1268.14/1410
60380.93	1.4 ± 0.2	96 ± 4	2.8 ± 0.3	0.07 ± 0.01	1.2E-07	30.6 ± 2.7	1.04 ± 0.01	1.01 ± 0.04	1195.73/1410
60381.75	1.4 ± 0.2	158 ± 3	2.6 ± 0.1	0.05 ± 0.01	4.3E-11	29.9 ± 2.4	1.05 ± 0.01	1.30 ± 0.06	1423.16/1411
60382.93	1.8 ± 0.1	45 ± 2	2.8 ± 0.2	0.18 ± 0.02	9.5E-15	31.9 ± 2.3	1.04 ± 0.02	1.09 ± 0.03	1353.27/1410
60383.85	1.9 ± 0.2	21 ± 1	2.8 ± 0.3	0.24 ± 0.02	2.0E-13	28.7 ± 2.3	0.99 ± 0.02	1.52 ± 0.12	1335.43/1410
60383.98	1.6 ± 0.1	40 ± 2	2.9 ± 0.3	0.13 ± 0.01	1.5E-12	28.8 ± 2.1	1.05 ± 0.02	1.06 ± 0.04	1327.92/1410
60384.12	1.6 ± 0.2	40 ± 3	2.9 ± 0.3	0.15 ± 0.02	2.2E-11	27.8 ± 2.8	1.04 ± 0.03	1.01 ± 0.03	1188.27/1409
60386.59	0.9 ± 0.3	1389 ± 23	3.4 ± 0.8	2.43 ± 0.23	3.7E-10	16.9 ± 3.2	1.00 ± 0.07	1.59 ± 0.16	1281.48/1410

Note. Column (1) represents the MJD of those respective Exposure IDs for which we have performed spectral analysis. Columns (2) and (3) give the values of the parameters from the diskbb model. Columns (4)–(7) give the values of the parameters from the pexriv model. Columns (8) and (9) give the values of the constants needed to achieve simultaneous broadband fitting. Column (10) gives the values of the χ^2/DOF for each fitting. For this model fitting, we have fixed the E_{cut} of this model to the E_{cut} of the pexrav model for fixed N_{H} . Also, the disk temperature was set to 10^6 K. Since, the ionization parameter ξ has so small value, we did not estimate the error for this parameter. The errors are estimated with a 90% confidence interval, which corresponds to 1.645σ in XSPEC.

correspondence). We find that on the last day of our analysis period, Γ became high (>3.3 from all three models). These values suggest that the source transitioned into the SS that day (R. A. Remillard & J. E. McClintock 2006). Thus, we did not find QPO in any band on that day. The absence of QPOs and high Γ agrees with the SS as inferred in S. Mondal et al. (2024) using joint IXPE and NuSTAR observations of the source. As mentioned previously in the result section, we have not noticed typical variations in Γ , $\text{Norm}_{\text{diskbb}}$, and T_{in} , and we have also found a broad range of the spin and inclination from the spectral analysis. We speculate that this is due to the contribution from the Cir X-1 source, albeit it was in the low-energy band.

We did not find the presence of any HFQPO during the entire analysis period of the outburst. The HFQPO phenomenon is not very common. To date, HFQPOs have been observed in a few sources only, e.g., GRO J1655-40 (R. A. Remillard et al. 1999; T. E. Strohmayer 2001b; R. A. Remillard & J. E. McClintock 2006), H1743-322 (J. Homan et al. 2005; Remillard et al. 2006), XTE J1550-564 (J. Homan et al. 2001; J. M. Miller et al. 2001; R. A. Remillard et al. 2002a), and GRS 1915 + 105 (E. H. Morgan et al. 1997; T. E. Strohmayer 2001b; T. Belloni et al. 2006). This suggests that this is not a very common phenomenon, like LFQPOs in BHXRBs. Their absence could be because the disk did not proceed very close to the compact object to produce variabilities with high frequency. Detection of HFQPOs requires high timing resolution and a large effective area, both of which are synonymous with the Insight-HXMT satellite. However, the photon statistics should be very strong to detect HFQPOs that require a very high S/N, especially in the soft energy band, as it is generally thought to be produced by the disk when it is very close to the BH. Considering this source was in proximity to another source, this may not have satisfied. These could be plausible causes for the nondetection of HFQPOs for this outburst. We also studied the energy dependence of LFQPOs in the HE band for those exposures in

which an LFQPO was present in the full energy band. The energy dependence of QPOs could give valuable insight into the origin of the QPO. X. Ma et al. (2023) reported that LFQPO was present until very high energy, which suggested that the origin of the QPO could be from the precession of the jet. Examining all 31 exposures, we find that LFQPO was present until 48 keV, above which there is no prominent or weak QPO nature, either. In the 27–35 keV band, the nature of LFQPOs was stronger than in the 35–48 keV band. Such observational findings can be explained from the TCAF model scenario, where in the intermediate states, CENBOL shrinks, due to the increase in cooling effects (see S. Mondal et al. 2015); therefore, the spectral break energy permissible for inverse Compton scattering also decreases, which is the case for the present source. Thereby, much higher energy photons possibly could not contribute to the observed QPOs. There could be another explanation for the absence of QPOs at high energies. We have noticed that the background count rates are higher for the HE band and are very comparable to the source count. Due to the high background, there could be less contribution from the source at higher energy bands. This could also explain why we do not observe QPOs at these HE bands. Since the source is already in the SIMS, the rms amplitude is generally lower than in the HS. Therefore, the upper limit on the rms amplitude cannot be constrained from the present data sets, requiring a detailed study with the complete cycle of an outburst.

The source Swift J151857.0-572147 has shown a very high value of N_{H} , using all three combinations of models. The N_{H} varied in the range $(4.3\text{--}6.5) \times 10^{22} \text{ cm}^{-2}$, $(5.1\text{--}6.3) \times 10^{22} \text{ cm}^{-2}$, and $(5\text{--}6.9) \times 10^{22} \text{ cm}^{-2}$ for Model-1, Model-2, and Model-3, respectively. The average column density was $\sim 5.6 \times 10^{22} \text{ cm}^{-2}$. This value is significantly higher compared to other Galactic BHs. For example, some BHCs Swift J1727.8-1613, MAXI J1803-298, GX 339-4, and Swift J1357.2-0933 the N_{H} varied in the range $(0.1\text{--}0.5) \times 10^{22} \text{ cm}^{-2}$ (K. Chatterjee et al. 2024; D. Debnath et al. 2024;

Table 11
Properties from Spectral Analysis Using Model-4 by Freezing the Column Density (N_{H}) to $5.6 \times 10^{22} \text{ cm}^{-2}$

Time MJD (1)	diskbb		relxill								Fitting Constants		Fitting Stat χ^2/DOF (14)
	T_{in} (keV) (2)	Norm (3)	Spin (4)	Incl. (i) (5)	Γ (6)	logxi (7)	AF_e (8)	E_{cut} (9)	rel _{frac} (10)	Norm (11)	Constant1 (12)	Constant2 (13)	
60373.90	1.54 ± 0.1	107 ± 2	0.81 ± 0.16	17 ± 4	2.4 ± 0.1	4.3 ± 0.1	1.5 ± 0.1	76 ± 3	0.45 ± 0.12	0.15 ± 0.01	1.07 ± 0.01	1.07 ± 0.02	1223.49/1406
60374.98	1.47 ± 0.1	146 ± 5	0.74 ± 0.11	19 ± 4	2.6 ± 0.1	4.5 ± 0.3	1.2 ± 0.1	145 ± 12	0.85 ± 0.21	0.20 ± 0.01	1.01 ± 0.02	1.02 ± 0.02	1246.18/1406
60375.94	1.56 ± 0.1	87 ± 3	0.81 ± 0.13	20 ± 3	2.6 ± 0.1	4.5 ± 0.2	1.4 ± 0.1	133 ± 11	0.91 ± 0.21	0.19 ± 0.01	1.05 ± 0.02	1.09 ± 0.03	1204.20/1406
60376.96	1.36 ± 0.1	411 ± 8	0.81 ± 0.11	24 ± 4	2.6 ± 0.1	4.3 ± 0.4	1.4 ± 0.1	97 ± 5	2.29 ± 0.19	0.07 ± 0.01	1.14 ± 0.03	1.18 ± 0.05	1311.53/1323
60377.98	1.24 ± 0.1	499 ± 8	0.81 ± 0.18	10 ± 3	2.4 ± 0.1	4.2 ± 0.3	1.1 ± 0.1	30 ± 1	1.75 ± 0.19	0.07 ± 0.01	1.07 ± 0.02	1.23 ± 0.08	1321.49/1406
60378.83	1.31 ± 0.1	314 ± 5	0.81 ± 0.13	12 ± 2	2.4 ± 0.1	4.3 ± 0.2	1.1 ± 0.1	33 ± 1	1.53 ± 0.10	0.08 ± 0.01	1.01 ± 0.01	1.36 ± 0.04	1592.23/1406
60379.84	1.34 ± 0.1	188 ± 4	0.81 ± 0.11	28 ± 2	2.4 ± 0.1	4.4 ± 0.2	1.3 ± 0.1	64 ± 1	1.54 ± 0.10	0.07 ± 0.01	1.02 ± 0.02	1.26 ± 0.04	1411.99/1406
60380.93	1.28 ± 0.1	208 ± 3	0.81 ± 0.32	36 ± 4	2.4 ± 0.1	4.7 ± 0.4	1.9 ± 0.3	56 ± 12	1.57 ± 0.17	0.07 ± 0.01	1.02 ± 0.02	1.11 ± 0.04	1325.13/1406
60381.75	1.46 ± 0.1	105 ± 3	0.65 ± 0.22	41 ± 5	2.8 ± 0.1	3.7 ± 0.6	1.6 ± 0.1	19 ± 1	1.26 ± 0.13	0.58 ± 0.01	1.05 ± 0.02	1.22 ± 0.06	1439.98/1407
60382.93	1.79 ± 0.1	30 ± 1	0.68 ± 0.22	37 ± 5	2.8 ± 0.1	3.9 ± 0.1	3.9 ± 0.1	32 ± 1	1.02 ± 0.17	0.52 ± 0.01	1.01 ± 0.01	1.22 ± 0.06	1355.12/1407
60383.85	1.90 ± 0.1	22 ± 1	0.50 ± 0.11	31 ± 3	2.8 ± 0.1	3.8 ± 0.1	1.7 ± 0.2	62 ± 1	0.12 ± 0.11	0.43 ± 0.01	1.01 ± 0.02	1.44 ± 0.01	1322.27/1406
60383.98	1.59 ± 0.1	37 ± 2	0.78 ± 0.22	29 ± 9	2.8 ± 0.1	4.1 ± 0.1	4.3 ± 0.7	143 ± 21	1.07 ± 0.16	0.45 ± 0.01	1.06 ± 0.02	1.06 ± 0.04	1323.12/1406
60384.12	1.50 ± 0.1	37 ± 2	0.50 ± 0.22	24 ± 1	2.8 ± 0.1	4.3 ± 0.1	4.9 ± 0.8	248 ± 53	1.40 ± 0.10	0.43 ± 0.01	1.06 ± 0.01	1.02 ± 0.04	1168.19/1406
60386.59	0.89 ± 0.1	1532 ± 17	0.50 ± 0.11	30 ± 1	3.0 ± 0.1	3.3 ± 0.1	3.8 ± 0.6	954 ± 408	0.82 ± 0.12	0.22 ± 0.01	1.11 ± 0.03	1.18 ± 0.09	1194.31/1406

Note. Column (1) represents the MJD of those respective Exposure IDs for which we have performed spectral analysis. Columns (2) and (3) give the values of the parameters from the diskbb model. Columns (4)–(11) give the values of the parameters from the relxill model. Columns (12) and (13) give the values of the constants needed to achieve simultaneous broadband fitting. Column (14) gives the values of the χ^2/dof for each fitting. The errors are estimated with a 90% confidence interval, which corresponds to 1.645σ in XSPEC.

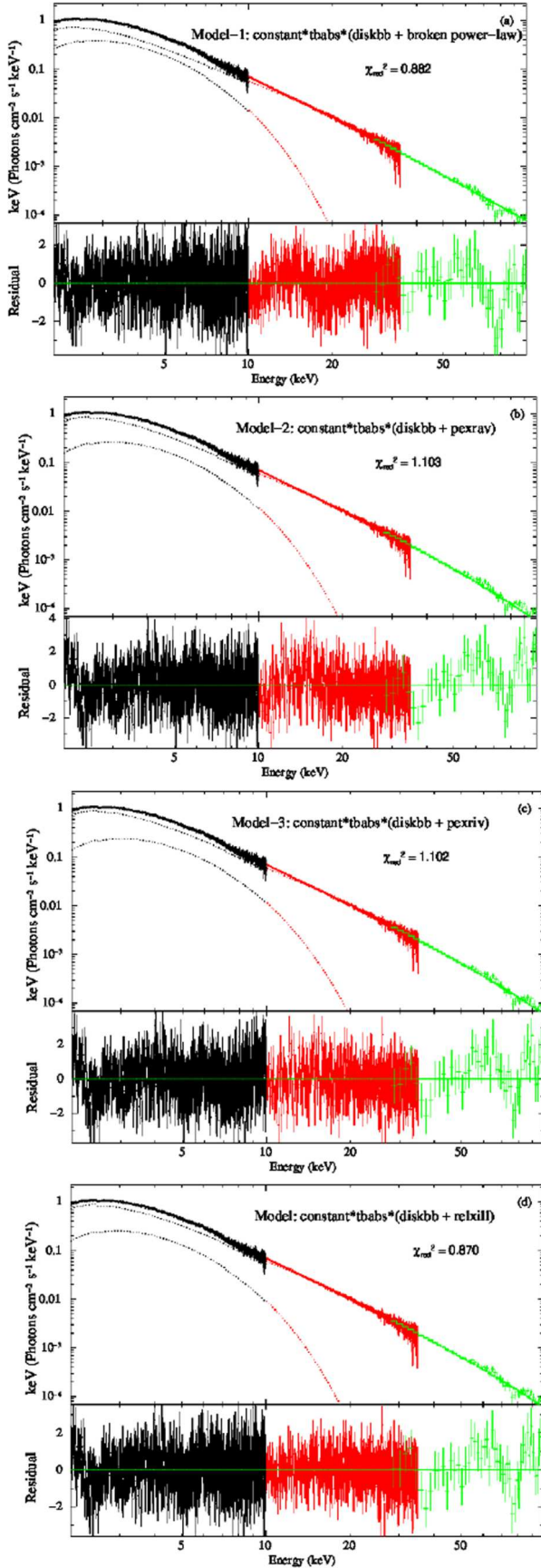


Figure 12. Best model-fitted unfolded spectra for observation ID. P0614374001 (Exposure: P061437400101-20240304-01-01) using (a) Model-1, (b) Model-2, (c) Model-3, and (d) Model-4.

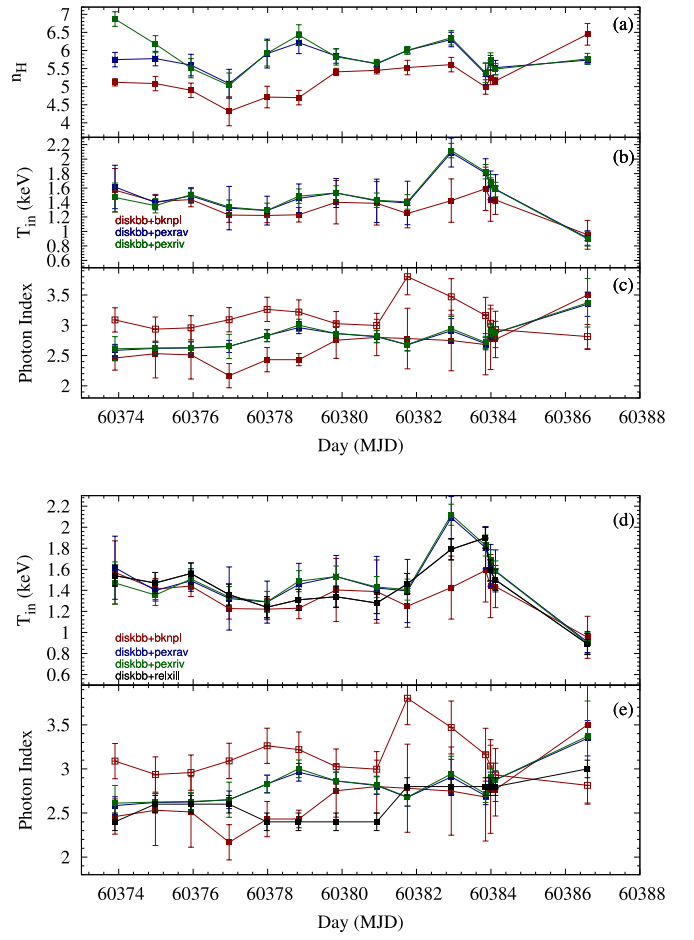


Figure 13. Best-fitted spectral model parameters are shown with time MJD. The panels (a), (b), and (c) show the variation in the hydrogen column density (in 10^{22} cm^{-2} unit), inner-disk temperature (T_{in} in keV), and photon index (Γ) for all three models. The red, blue, and green colors represent the parameters for Model-1, Model-2, and Model-3, respectively. In the panel (c), we show the Γ_1 and Γ_2 of Model-1 using red color filled and empty squares, respectively. The panels (d) and (e) represent the same parameters as in panels (b) and (c), but for the N_{H} fixed to $5.6 \times 10^{22} \text{ cm}^{-2}$.

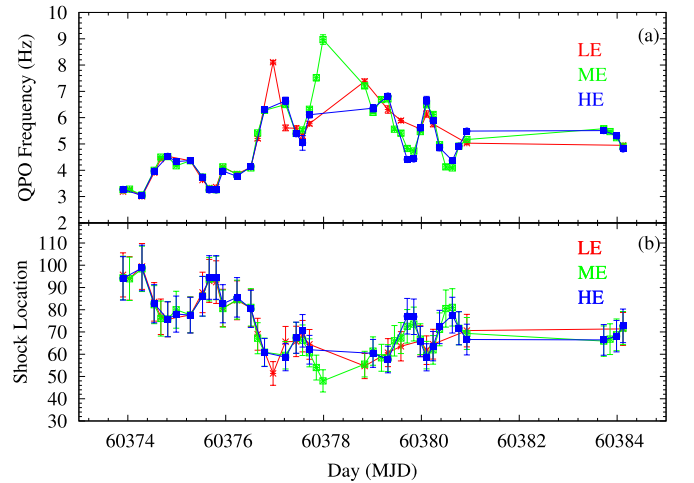


Figure 14. Evolution of the location of the shock, estimated from observed ν_{qpo} . Panel (a) shows the variation in ν_{qpo} with time, and panel (b) shows the variation in X_s with time.

H.-X. Liu et al. 2024), $(0.2-0.5) \times 10^{22} \text{ cm}^{-2}$ (A. Jana et al. 2022; O. K. Adegoke et al. 2024), $0.5 \times 10^{22} \text{ cm}^{-2}$ (S. Motta et al. 2009), and $0.13 \times 10^{22} \text{ cm}^{-2}$ (S. Mondal & S. K. Chakrabarti 2019). For these sources, there was no local absorption and thus the values were close to the Galactic hydrogen column density (HI4PI Collaboration 2016). This has also been observed for other BHXRBs for which there was no local absorption to the source. This indicates some absorption local to the source, which could be due to the outflows from the disk or the presence of some blobs along the line of sight (see J. Neilsen & J. Homan 2012; S. Mondal & V. Jithesh 2023). To confirm this, we need a detailed study of the outflow/jet properties of the source.

5. Summary and Conclusions

We have studied the timing and spectral properties of the very first outburst of the BHC Swift J151857.0-572147 in 2024. Using Insight-HXMT LE, ME, and HE exposure average light curve data, we present the evolution of the light curve and its HR across our full analysis period from 2024 March 4 (MJD 60373) to 2024 March 17 (MJD 60386). For our investigation, we selected the seven observation IDs using the Insight-HXMT data, publicly available during the analysis. For timing analysis, we employed all of the exposures from those observation IDs, and for spectrum analysis, we employed selective exposures, respectively. We produced a power density spectrum and used 0.01 s time-binned light curves from the three HXMT instruments, i.e., LE, ME, and HE, to study the QPO properties. We used the Lorentzian model to obtain the QPO properties. We also studied energy-dependent QPO by producing HE light curves in seven different energy bands. We extracted the energy-dependent QPO properties in the same way we did for the LE, ME, and HE light curves in the full band. Apart from these, we also produced a 0.001 s time-binned light curve to search for HFQPOs. We employ LE + ME + HE spectrum files in the broad 2–100 keV energy band for spectral analysis. We found that the models (i) constant * tbabs * (diskbb + broken power law) and (ii) constant * tbabs * (diskbb + pexrav) fit the spectra for the best statistics. Based on our investigation, we conclude that:

(i) The source was present in the intermediate state at the start of our analysis period and proceeded toward the SS as the outburst progressed.

(ii) It was in the SS at the last observation ID of our analysis period.

(iii) Type-C QPO was present in the intermediate state, which could be produced by the shock instability in the transonic accretion flow.

(iv) As the source transitioned to the SS, we did not find any QPOs.

(v) LFQPOs were present up to 48 keV, above which we did not find the presence of LFQPO for any of the exposures.

(vi) HFQPOs were absent during this analysis period.

(vii) As the shock was of intermediate strength, it could not produce variabilities up to very high energies. Thus, we only found QPOs up to 48 keV.

(viii) The average hydrogen column density was high with $N_{\text{H}} \sim 5.6 \times 10^{22} \text{ cm}^{-2}$ in accordance with the estimation by S. Mondal et al. (2024) and J.-Q. Peng et al. (2024). This could be due to the presence of outflows from the disk or some blobs along the line of sight, which prompts a further detailed study.

Acknowledgments

We thank Dr. Lian Tao of the Institute of High Energy Physics (IHEP), Chinese Academy of Sciences (CAS), for publicizing the Insight-HXMT data by request. We also thank Dr. Mutsumi Sugizaki of Kanazawa University, Japan, for providing fruitful information about the absence of the MAXI/GSC daily average light curve on the source. We sincerely thank Prof. John A. Tomsick of the Space Sciences Lab, University of California, Berkeley, USA, for providing suggestions on the draft. C.B.S. is supported by the National Natural Science Foundation of China under grant No. 12073021. S.P.S. and S.M. acknowledge the Ramanujan Fellowship (RJF/2020/000113) by SERB/ANRF-DST, Govt. of India, for this research. K.C. acknowledges support from the SWIFAR postdoctoral fund of Yunnan University.

Data Availability

This work has made use of public data from several satellite/instrument archives and has made use of software from the HEASARC, which is developed and monitored by the Astrophysics Science Division at NASA/GSFC and the High Energy Astrophysics Division of the Smithsonian Astrophysical Observatory. This work made use of the data from the Insight-HXMT mission, a project funded by the China National Space Administration (CNSA) and the Chinese Academy of Sciences (CAS).

Appendix

Before fitting the data with the combination of phenomenological broken-power-law or physical pexrav models with the combination of the diskbb model, we tried to perform the spectral analysis using only the combination of diskbb and power-law models with the interstellar absorption model tbabs. The model combination reads as: constant * tbabs (diskbb + power law). However, from Figure 15, we notice that at the high-energy end, after 20 keV, there is the presence of high residuals, which could be due to the presence of reflection radiation. Thus, we modeled the data using the above-mentioned models to better fit the data, which we achieved.

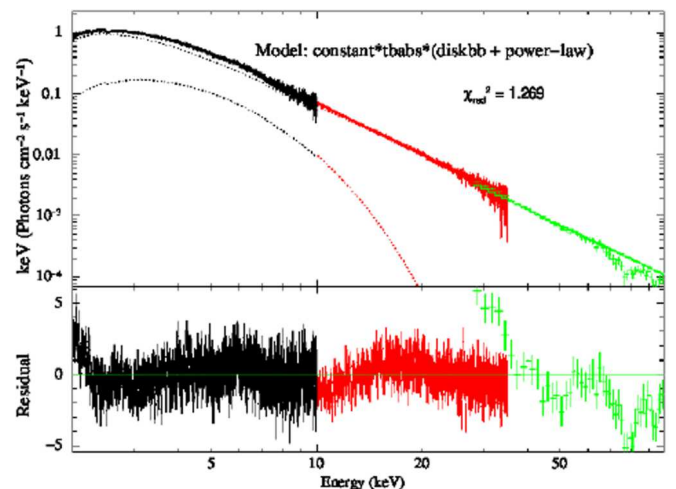


Figure 15. Model-fitted unfolded spectrum for the combination of tbabs, diskbb, and power-law models. This is for the observation ID. P0614374001 (exposure ID: P061437400101-20240304-01-01).

ORCID iDs

Kaushik Chatterjee  <https://orcid.org/0000-0002-6252-3750>
 S. Pujitha Suribhatla  <https://orcid.org/0009-0002-3317-5213>
 Santanu Mondal  <https://orcid.org/0000-0003-0793-6066>
 Chandra B. Singh  <https://orcid.org/0000-0002-7782-5719>

References

- Adegoke, O. K., Garcia, J. A., Connors, R. M. T., et al. 2024, *ApJ*, **977**, 26
 Baglio, M. C., D'Avanzo, P., Ferro, M., Campana, S., & Covino, S. 2024, *ATel*, **16506**, 1
 Bellavita, C., Garcia, F., Méndez, M., & Karpouzas, K. 2022, *MNRAS*, **519**, 2099
 Belloni, T., Homan, J., Casella, P., et al. 2005, *A&A*, **440**, 207
 Belloni, T., Psaltis, D., & van der Klis, M. 2002, *ApJ*, **572**, 392
 Belloni, T., Soleri, P., Casella, P., Méndez, M., & Migliari, S. 2006, *MNRAS*, **369**, 305
 Bu, Q.-C., Li, Z.-S., Qu, J.-L., Belloni, T. M., & Zhang, L. 2015, *ApJ*, **799**, 2
 Burridge, B. J., Miller-Jones, J. C. A., Bahramian, A., et al. 2024, *ATel*, **16538**, 1
 Cabanac, C., Henri, G., Petrucci, P.-O., et al. 2010, *MNRAS*, **404**, 738
 Carotenuto, F., Russell, T. D. & JACKPOT Collaboration 2024, *ATel*, **16518**, 1
 Casella, P., Belloni, T., & Stella, L. 2005, *ApJ*, **629**, 403
 Chakrabarti, S. K. 1989, *MNRAS*, **340**, 7
 Chakrabarti, S. K., Debnath, D., Nandi, A., & Pal, P. S. 2008, *A&A*, **489**, L41
 Chakrabarti, S. K., Mondal, S., & Debnath, D. 2015, *MNRAS*, **452**, 3451
 Chakrabarti, S. K., Nandi, A., Debnath, D., Sarkar, R., & Datta, B. G. 2005, *arXiv:0508024*
 Chakrabarti, S. K., & Titarchuk, L. G. 1995, *ApJ*, **455**, 623
 Chatterjee, K., Debnath, D., Chatterjee, D., Jana, A., & Chakrabarti, S. K. 2020, *MNRAS*, **493**, 2452
 Chatterjee, K., Debnath, D., Chatterjee, D., et al. 2021, *Ap&SS*, **366**, 63
 Chatterjee, K., Debnath, D., Nath, S. K., & Chang, H.-K. 2023, *ApJ*, **965**, 55
 Chatterjee, K., Mondal, S., Singh, C. B., & Sugizaki, M. 2024, *ApJ*, **977**, 148
 Chen, W., Shrader, C. R., & Livio, M. 1997, *ApJ*, **491**, 312
 Cowie, F. J., Carotenuto, F., Fender, R. P., et al. 2024, *ATel*, **16503**, 1
 Dauser, T., Garcia, J., Walton, D. J., et al. 2016, *A&A*, **590**, A76
 Debnath, D., Chakrabarti, S. K., & Nandi, A. 2010, *A&A*, **520**, A98
 Debnath, D., Mondal, S., & Chakrabarti, S. K. 2015, *MNRAS*, **447**, 1984
 Debnath, D., Nath, S. K., Chatterjee, D., Chatterjee, K., & Chang, H.-K. 2024, *ApJ*, **975**, 194
 Del Santo, M., Russell, T. D., Marino, A., & Motta, S. 2024, *ATel*, **16519**, 1
 Done, C., Mulchaey, J. S., Mushotzky, R. F., & Arnaud, K. A. 1992, *ApJ*, **395**, 275
 Fender, R. P., Belloni, T. M., & Gallo, E. 2004, *MNRAS*, **355**, 1105
 Ferreira, J. 1997, *A&A*, **319**, 340
 Ferreira, J., Marcel, G., Petrucci, P.-O., et al. 2022, *A&A*, **660**, A66
 Frank, J., King, A., & Raine, D. 2002, *Accretion Power in Astrophysics* (Cambridge: Cambridge Univ. Press)
 Garain, S., Ghosh, H., & Chakrabarti, S. K. 2014, *MNRAS*, **437**, 1329
 García, F., Karpouzas, K., Méndez, M., et al. 2022, *MNRAS*, **513**, 419
 Giannios, D., Kylafis, N. D., & Psaltis, D. 2004, *A&A*, **425**, 163
 Hannikainen, D. C., Charles, P. A., van Zyl, L., et al. 2005, *MNRAS*, **357**, 325
 HI4PI Collaboration 2016, *A&A*, **594**, A116
 Homan, J., Miller, J. M., Wijnands, R., et al. 2005, *ApJ*, **623**, 383
 Homan, J., Wijnands, R., van der Klis, M., et al. 2001, *ApJS*, **132**, 377
 Ichimaru, S. 1977, *ApJ*, **214**, 840
 Ingram, A., Done, C., & Fragile, P. C. 2009, *MNRAS*, **397**, L101
 Ingram, A., & Motta, S. 2019, *NewAR*, **85**, 101524
 Jana, A., Debnath, D., Chakrabarti, S. K., Mondal, S., & Molla, A. A. 2016, *ApJ*, **819**, 107
 Jana, A., Naik, S., Jaiswal, G., et al. 2022, *MNRAS*, **511**, 3922
 Karpouzas, K., Méndez, M., García, F., et al. 2021, *MNRAS*, **503**, 5522
 Kato, S. 2001, *PASJ*, **53**, 1
 Kato, S., & Fukue, J. 1980, *PASJ*, **32**, 377
 Kennea, J. A., Lien, A. Y., D'Elia, V., et al. 2024, *ATel*, **16500**, 1
 Kylafis, N. D., Reig, P., & Papadakis, I. 2020, *A&A*, **640**, L16
 Leahy, D. A., Darbro, W., Elsner, R. F., et al. 1983, *ApJ*, **266**, 160L
 Li, L.-X., Zimmerman, E. R., Narayan, R., & McClintock, J. E. 2005, *ApJS*, **157**, 335
 Liu, H.-X., Xu, Y.-J., Zhang, S.-N., Yu, W., et al. 2024, *arxiv:2406.03834*
 Ma, X., Zhang, L., Bu, Q. C., Qu, J. L., Zhang, S. N., et al. 2023, *ApJ*, **948**, 116
 Marcel, G., Ferreira, J., Clavel, M., et al. 2019, *A&A*, **626**, A115
 Mastroserio, G., Ingram, A., Wang, J., et al. 2021, *MNRAS*, **507**, 55
 McClintock, J. E., Narayan, R., & Steiner, J. F. 2014, *SSRv*, **183**, 295
 Miller, J. M., Wijnands, R., Homan, J., et al. 2001, *ApJ*, **563**, 928
 Molteni, D., Sponholz, H., & Chakrabarti, S. K. 1996, *ApJ*, **457**, 805
 Mondal, S., & Chakrabarti, S. K. 2013, *MNRAS*, **431**, 2716
 Mondal, S., & Chakrabarti, S. K. 2019, *MNRAS*, **483**, 1178
 Mondal, S., & Chakrabarti, S. K. 2021, *ApJ*, **920**, 41
 Mondal, S., Chakrabarti, S. K., & Debnath, D. 2015, *ApJ*, **798**, 57
 Mondal, S., Debnath, D., & Chakrabarti, S. K. 2014, *ApJ*, **786**, 4
 Mondal, S., & Jithesh, V. 2023, *MNRAS*, **522**, 2065
 Mondal, S., Suribhatla, S. P., Chatterjee, K., Singh, C. B., & Chatterjee, R. 2024, *ApJ*, **975**, 257
 Morgan, E. H., Remillard, R. A., & Greiner, J. 1997, *ApJ*, **482**, 993
 Motta, S., Belloni, T., & Homan, J. 2009, *MNRAS*, **400**, 1603
 Motta, S., Muñoz-Darias, T., Casella, P., et al. 2011, *MNRAS*, **418**, 2292
 Muñoz-Darias, T., Motta, S., & Belloni, T. M. 2011, *MNRAS*, **410**, 679
 Narayan, R., & Yi, I. 1994, *ApJL*, **428**, L13
 Neilsen, J., & Homan, J. 2012, *ApJ*, **750**, 27
 Nowak, M.A. 2000, *MNRAS*, **318**, 361
 Paczynski, B., & Wiita, P. 1980, *A&A*, **88**, 23
 Peng, J.-Q., Zhang, S., Shui, Q.-C., et al. 2024, *ApJL*, **973**, L7
 Petrucci, P.-O., Ferreira, J., Henri, G., & Pelletier, G. 2008, *MNRAS*, **385**, L88
 Psaltis, D., Belloni, T., & van der Klis, M. 1999, *ApJ*, **520**, 262
 Reig, P., Kylafis, N. D., & Giannios, D. 2003, *A&A*, **403**, L15
 Remillard, R. A., & McClintock, J. E. 2006, *ARA&A*, **44**, 49
 Remillard, R. A., Morgan, E. H., McClintock, J. E., Bailyn, C. D., & Orosz, J. A. 1999, *ApJ*, **522**, 397
 Remillard, R. A., Sobczak, G. J., Munro, M. P., & McClintock, J. E. 2002a, *ApJ*, **564**, 962
 Ryu, D., Chakrabarti, S. K., & Molteni, D. 1997, *ApJ*, **474**, 378
 Saikia, P., Russell, D. M., Baglio, M. C., et al. 2024, *ATel*, **16516**, 1
 Sguera, V. 2024, *ATel*, **16524**, 1
 Shakura, N. I., & Sunyaev, R. A. 1973, *A&A*, **24**, 337
 Sreehari, H., Ravishankar, B. T., Iyer, N., et al. 2019, *MNRAS*, **487**, 928
 Stella, L., Vietri, M., & Morsink, S. M. 1999, *ApJL*, **524**, L63
 Strohmayer, T. E. 2001b, *ApJL*, **554**, L169
 Sunyaev, R. A., & Titarchuk, L. G. 1980, *A&A*, **86**, 121
 Sunyaev, R. A., & Titarchuk, L. G. 1985, *A&A*, **143**, 374
 Tagger, M., & Pellat, R. 1999, *A&A*, **349**, 1003
 Tetarenko, B. E., Sivakoff, G. R., Heinke, C. O., & Gladstone, J. C. 2016, *ApJS*, **222**, 15
 Thorne, K. S., & Price, R. H. 1975, *ApJL*, **195**, L101
 Titarchuk, L., Lapidus, I., & Muslimov, A. 1998, *ApJ*, **499**, 315
 Tsang, D., & Butsky, I. 2013, *MNRAS*, **435**, 749
 van der Klis, M. 1989, *ARA&A*, **27**, 517
 Wagoner, R.V. 1999, *PhR*, **311**, 259
 Wilms, J., Allen, A., & McCray, R. 2000, *ApJ*, **542**, 914
 Zhang, G. B., Bernardini, F., Russell, D. M., et al. 2019, *ApJ*, **876**, 5
 Zhang, S.-N., Li, T., Lu, F., et al. 2020, *SCPMA*, **63**, 249502